

Real-time adaptive tracking of fluctuating relaxation rates in superconducting qubits

Fabrizio Berritta,^{1,2,*} Jacob Benestad,³ Jan A. Krzywda,⁴ Oswin Krause,⁵ Malthe A. Marciniak,^{1,2} Svend Krøjer,^{1,2} Christopher W. Warren,^{6,1,2} Emil Hogedal,⁶ Andreas Nylander,⁶ Irshad Ahmad,⁶ Amr Osman,⁶ Janka Biznárová,⁶ Marcus Rommel,⁶ Anita Fadavi Roudsari,⁶ Jonas Bylander,⁶ Giovanna Tancredi,⁶ Jeroen Danon,³ Jacob Hastrup,^{1,2} Ferdinand Kuemmeth,^{1,7,8} and Morten Kjaergaard^{1,2,†}

¹Center for Quantum Devices, Niels Bohr Institute, University of Copenhagen, 2100 Copenhagen, Denmark

²NNF Quantum Computing Programme, Niels Bohr Institute, University of Copenhagen, 2100 Copenhagen, Denmark

³Center for Quantum Spintronics, Department of Physics, Norwegian University of Science and Technology, NO-7491 Trondheim, Norway

⁴Lorentz Institute for Theoretical Physics & Leiden Institute of Advanced Computer Science, Universiteit Leiden, 2311 EZ Leiden, The Netherlands

⁵Department of Computer Science, University of Copenhagen, 2100 Copenhagen, Denmark

⁶Department of Microtechnology and Nanoscience, Chalmers University of Technology, SE-412 96 Gothenburg, Sweden

⁷Institute of Experimental and Applied Physics, University of Regensburg, 93040 Regensburg, Germany

⁸QDevil, Quantum Machines, 2750 Ballerup, Denmark

(Dated: February 13, 2026)

The fidelity of operations on a solid-state quantum processor is fundamentally bounded by environmental decoherence. Characterizing environmental fluctuations is challenging because the acquisition time of nonadaptive experimental protocols limits temporal precision and can average out rapid features of the underlying dynamics. Here, we overcome this temporal-resolution limit by two orders of magnitude using a field-programmable gate-array (FPGA) powered classical controller that adaptively and continuously tracks the relaxation-time fluctuations of two fixed-frequency superconducting transmon qubits, which exhibit average relaxation times of approximately 0.17 ms and occasionally exceed 0.5 ms. We report events in which the relaxation time switches by nearly an order of magnitude over timescales of just tens of milliseconds, rather than minutes or hours as previously reported. Our real-time Bayesian estimation protocol estimates relaxation times within a few milliseconds, close to the decoherence timescale itself. Our statistical analysis further suggests that some of these fast fluctuations arise from two-level systems switching at rates up to 10 Hz, four orders of magnitude faster than earlier reports. These results redefine the timescales relevant for calibration in superconducting quantum processing units, establish a reference for rapid relaxation-rate characterization in device screening, and improve our understanding of fast relaxation dynamics.

I. INTRODUCTION

Superconducting qubits [1–5] are among the main candidates for fault-tolerant quantum computation schemes, with quantum operations on these devices approaching error rates capable of demonstrating quantum error correction [6–9]. However, as the number of physical qubits increases in quantum processing units (QPUs), the QPU’s performance is bounded by the lowest-performing outlier qubits [10–12]. Identifying such outliers can be nontrivial, as time-dependent fluctuations in physical qubit parameters may alter which qubits qualify as outliers at any given moment. This is complicated by the physical mechanisms for these variations drifting over several different and competing timescales. In particular, the relaxation rate T_1 of a superconducting qubit directly limits the fidelity of quantum operations [13]. T_1 fluctuates unpredictably in the time domain [14–22] and also as

a function of the qubit frequency [14–18, 22, 23]. One of the major contributions to energy relaxation in state-of-the-art superconducting qubits is frequently attributed to their (semi-)resonant interaction with environmental two-level system (TLS) defects [14, 15, 24], though their detailed microscopic origins remain unknown. It has been shown that TLS frequencies drift over repeated cooldowns, whereas the overall number of TLSs does not [20, 25].

Previous works in transmon qubits have resolved T_1 with a time resolution of seconds [18, 26, 27] or minutes [28, 29]. More efficient and scalable estimation methods are needed to (i) probe previously unexplored sub-second regimes of T_1 dynamics, which is necessary for understanding the underlying physics, and (ii) identify outlier qubits and time-dependent fluctuations [14–16, 24] in large QPUs to ensure fast and reliable characterization and error mitigation. Modern field-programmable gate array (FPGA) advancements have facilitated *online* (during experimental data collection) Hamiltonian learning [30, 31], which is a useful tool to probe drifts in qubit parameters through real-time estimation [31–40].

In this work, we investigate fast fluctuations of the relaxation rates of two long-lived transmon qubits (with

* Current address: Research Laboratory of Electronics, Massachusetts Institute of Technology, Cambridge, MA 02139, USA; fabrizio.berritta@mit.edu

† mkjaergaard@nbi.ku.dk

$T_1 \equiv 1/\Gamma_1 \approx 0.17$ ms measured over several hours) on millisecond timescales, almost comparable to the relaxation times themselves. We use a commercial controller with an integrated FPGA that leverages single-shot readout and performs real-time Bayesian estimation of the relaxation time, overcoming the sampling limitations of the traditional method mentioned below by two orders of magnitude. Our adaptive estimation allows the controller to investigate the stochastic behavior of the relaxation rate on unprecedentedly short timescales, revealing events where the relaxation time switches by almost an order of magnitude on the timescale of tens of milliseconds, instead of minutes or hours [14–16]. We analyze the fluctuations of Γ_1 using the power spectral density and Allan deviation [41] and find that a simple Lorentzian model describes the observed fluctuations, allowing us to extract TLS switching rates as fast as 10 Hz, $10^4 \times$ faster than previously reported, and to monitor changes in the dominating TLS environment with sub-minute time resolution.

To appreciate the advantages of our approach, it is useful to recall the traditional protocol. The most common method for estimating Γ_1 consists of initializing the qubit to the excited state and measuring its state projectively after a fixed (*nonadaptive*) waiting time. For each waiting time τ_{wait} , the measurement outcome is averaged over many repetitions, and this is repeated for all waiting times. The fraction of times the system is measured in the excited state as a function of waiting time is then fitted to an exponential decay $\propto e^{-\Gamma_1 \tau_{\text{wait}}}$. The drawbacks of such a nonadaptive method are that (i) it is not optimally efficient in terms of experiment time, (ii) prior estimates of the qubit’s Γ_1 are not used to track its subsequent temporal fluctuations, and (iii) implementing curve fitting directly on an FPGA is challenging due to the available numerical precision, which prevents interleaving such estimations with qubit operations in real time.

Bayesian parameter estimation [31, 42] instead is a natural approach to implementing real-time optimization techniques [31, 34, 35, 38–40] compatible with low-latency control hardware. By using an onboard probability distribution of the parameter estimate, the optimal experimental settings for each subsequent probing cycle may be chosen *adaptively* so as to maximize the knowledge obtained from every (single-shot) measurement. In this work the technique is validated with shot-by-shot interleaved estimations of the relaxation time using our Bayesian method and the traditional approach.

Our scheme sets a new reference for fast QPU characterization of relaxation rates, for probing relaxation dynamics at previously unexplored time resolution, and is well suited for stable interleaved QPU execution in the presence of Γ_1 fluctuations.

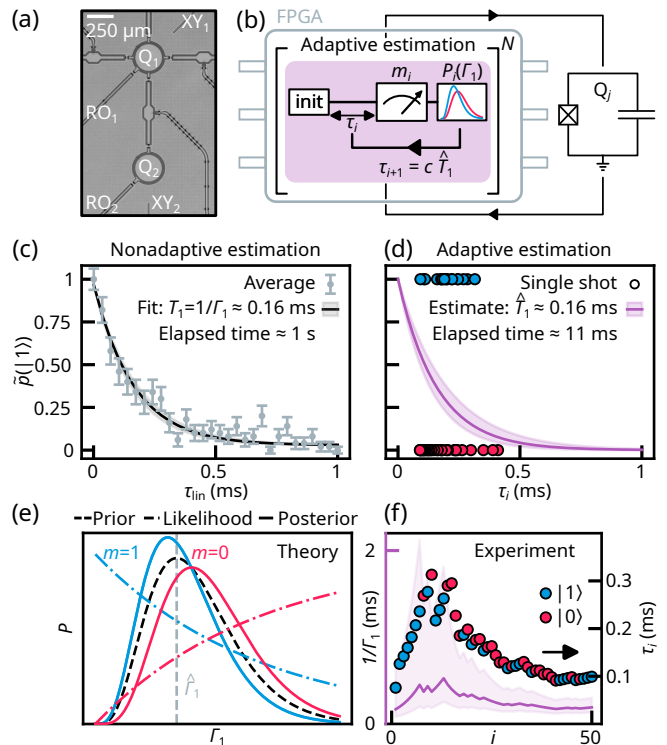


FIG. 1. Device and Bayesian adaptive decay-rate estimation. (a) Optical micrograph of transmon qubits (Q_1 and Q_2) nominally identical to the ones used in this work. Each transmon (Q_j) is individually controlled by microwave pulses (XY_j) and read out through independent resonators (RO_j). (b) Experimental scheme for adaptively estimating the qubit decay rate Γ_1 (purple box) on the FPGA in real time over N probe cycles. In each cycle, labeled i , the controller initializes Q_j to the excited state (init), waits a time τ_i adaptively chosen based on $\hat{T}_1 \equiv 1/\langle \Gamma_1 \rangle$ from the previous Bayesian distribution $\mathcal{P}_{i-1}(\Gamma_1)$, then updates the probability distribution $\mathcal{P}_i(\Gamma_1)$ based on the measurement outcome m_i . (c) Example of a nonadaptive estimation of the relaxation time. From the normalized fraction $\hat{p}(|1\rangle)$ of excited states as a function of linearly stepped probing waiting times τ_{in} , Γ_1 is estimated by an exponential fit. The total elapsed time is ≈ 1 s. (d) Example of an adaptive estimation of \hat{T}_1 by Bayesian statistics implemented on the controller. Each circle is a single-shot measurement outcome $|0\rangle$ (red) or $|1\rangle$ (blue) which updates the current estimate of \hat{T}_1 and the subsequent adaptive waiting time τ_i . The total elapsed time for the entire estimation is ≈ 11 ms. (e) Evolution of the probability distribution \mathcal{P} during each probe cycle i of the estimation algorithm. The current estimate is $\hat{\Gamma}_1$ (gray dashed line). On each probing cycle, the estimate of $\hat{\Gamma}_1$ is updated according to two possible likelihood functions (dot-dashed lines), multiplied by the prior distribution (dashed). This yields the posterior distribution (solid), whose estimate is shifted left or right depending on the measurement outcome, while the uncertainty is reduced on average. (f) Convergence of \mathcal{P} as a function of the i^{th} probe cycle. The line shows the resulting estimate \hat{T}_1 and the shaded area marks the 90% credible interval. As in panel (d), each circle is a single-shot outcome m_i with corresponding waiting time τ_i .

II. SETUP AND PROTOCOL

We use a 5-qubit superconducting array with tunable couplers operated at the mixing-chamber stage (below 10 mK) of a dilution refrigerator. The device design and fabrication is similar to Ref. [43]. We implement the decay-rate estimation protocol on two of the five available qubits. In the main text, we focus on a transmon qubit (Q_1) of frequency ≈ 4.13 GHz and anharmonicity ≈ -210 MHz, as shown in Fig. 1(a). The results from another qubit (Q_2) in the same device are presented in the Supplemental Material [44]. In our qubits, the expected Purcell-limited relaxation time is ≈ 0.8 ms. A commercial controller (Quantum Machines OPX1000) applies microwave pulses for qubit control and single-shot readout, using dedicated XY control lines and readout resonators respectively [See Fig. 1(a)] [1–5].

The fluctuating parameter Γ_1 is estimated on the FPGA from the probing sequence shown in Fig. 1(b). For each probe cycle (labeled $1 \leq i \leq N$), the qubit is initialized to the ground state $|0\rangle$ via active reset [45] and is then brought to the excited state $|1\rangle$ using an X_π pulse. After waiting for an adaptive waiting time τ_i , the controller assigns the qubit state as ground ($m_i = 0$) or excited ($m_i = 1$) by thresholding the demodulated dispersive readout signal. The Bayesian probability distribution $\mathcal{P}_i(\Gamma_1)$, detailed in Sec. III, is updated based on m_i . The controller then uses the updated estimate of $\hat{T}_1 \equiv 1/\langle\Gamma_1\rangle$ based on $\mathcal{P}_i(\Gamma_1)$ and selects a new waiting time $\tau_{i+1} = c\hat{T}_1$, with c fixed, for the subsequent probing cycle.

To contrast our estimation method with the standard (nonadaptive) approach, we first present in Fig. 1(c) a “standard T_1 experiment”. For clarity, the measurement outcomes of Fig. 1(c-d) ignore readout errors. Specifically, in Fig. 1(c) we plot the normalized measured fractions of excited states, $\tilde{p}(|1\rangle)$ as a function of the linear waiting time τ_{in} , along with the corresponding exponential fit, yielding a decay constant of $T_1 = 1/\Gamma_1 = (165 \pm 15)$ μs . This experiment is based on 1,890 single-shot measurements and spans approximately one second, comparable to the method used in Ref. [26].

In contrast, in Figure 1(d), we present a representative run of our adaptive approach. The controller uses 50 single-shot measurement outcomes (experiment performed the day after the nonadaptive one), each of which is used to update the probability distribution on the controller iteratively. The updated distribution is then used to calculate an adaptive waiting time for the subsequent probing shot. After 50 single-shot measurements, the estimated value is $\hat{T}_1 \approx 159$ μs , with a 68% credible interval (CI) of $[131, 202]$ μs , and a total elapsed time of only 11 ms ($\approx 69\hat{T}_1$). The purple curve illustrates the corresponding exponential decay, the shaded area indicating the CI.

We see that the resulting uncertainty from the adaptive method is slightly larger than the nonadaptive case, while the estimator \hat{T}_1 was obtained with a total estimation

time that is two orders of magnitude shorter. Moreover, in Fig. 1(c), the chosen values of waiting times within the interval $[1, 1000]$ μs are appropriate for the estimated relaxation time in this specific example. However, if T_1 were to fluctuate drastically, a nonadaptive estimation on the same grid would result in a much greater uncertainty. The adaptive scheme is much more robust to these fluctuations as the waiting times are selected dynamically (for further details on how the adaptive method outperforms the nonadaptive one, see the Supplemental Material [44]).

III. BAYESIAN ESTIMATION

We now describe our efficient and adaptive Bayesian estimation method for the decay rate implemented on the controller. The crux of the protocol is that all information about the current estimate of the probability distribution, $\mathcal{P}(\Gamma_1)$, is stored at any time, dynamically and with only a few parameters, on the controller. This on-controller parametrization allows each Bayesian update of $\mathcal{P}(\Gamma_1)$ to take only ≈ 2.2 μs (cf. the update time of ≈ 50 μs in Ref. [34], which used particle filtering for estimating decoherence rates in a nitrogen-vacancy center). Section IV presents our main results on Γ_1 estimation, which remain accessible without reference to the following implementation details.

An overview of our Bayesian estimation method was described in the previous section, however we reiterate to be explicit as to what is executed at every step of the protocol and its approximations. The estimation method involves a probing cycle where the qubit is first initialized in the excited state $|1\rangle$. This initialization is followed by a waiting time τ after which the state of the qubit is measured using dispersive readout. Since the fluctuations of $\Gamma_1(t)$ tend to be dominated by low-frequency noise [14, 15], we approximate $\Gamma_1(t)$ to be quasistatic on the scale of tens of probing cycles (i.e., a few ms). In the following, we thus drop the time dependence of $\Gamma_1(t)$ for ease of notation.

We assume that after the initialization the probability of measuring an outcome $m \in \{0, 1\}$ corresponding to the states $|0\rangle$ and $|1\rangle$ is given by the likelihood function [dot-dashed lines in Fig. 1(e)]

$$P(m|\Gamma_1, \tau) = 1 - m - (-1)^m[\beta + (1 - \alpha - \beta)e^{-\Gamma_1\tau}], \quad (1)$$

where Γ_1 is the parameter we want the controller to estimate, and α and β are misclassification probabilities for measuring $|0\rangle$ when at the beginning of the measurement the true state is $|1\rangle$ and measuring $|1\rangle$ when the true state is $|0\rangle$, respectively [46].

In the quasistatic approximation, by Bayes’ rule, one obtains

$$\mathcal{P}_{i+1}(\Gamma_1) \propto \mathcal{P}_i(\Gamma_1)P(m_{i+1}|\Gamma_1, \tau_{i+1}), \quad (2)$$

where the prior $\mathcal{P}_i(\Gamma_1)$ describes the probability distribution for Γ_1 after the i^{th} probing cycle, which depends

on all the previously used waiting times and measurement outcomes, and the posterior $\mathcal{P}_{i+1}(\Gamma_1)$ describes the distribution after the subsequent cycle.

A simple parametrization of probability distributions is generally favorable in Bayesian approaches for on-FPGA optimization and computational speed, as demonstrated in Ref. [40]. In typical experiments, the distribution of estimated Γ_1 's fits well to a Gaussian [29], which suggests approximating the prior and posterior in Eq. (2) by a Gaussian for all i [40, 47]. However, combining a Gaussian prior with the exponential likelihood function in Eq. (1) results in a posterior that is not well approximated by a Gaussian distribution, especially when the spread of the Gaussian becomes comparable to its mean, yielding also the unphysical ingredient of significant probability for negative values of Γ_1 .

Instead, we find that the gamma distribution is a convenient choice,

$$\mathcal{P}_i(\Gamma_1|k_i, \theta_i) = \frac{\theta_i^{k_i}}{\Gamma(k_i)} \Gamma_1^{k_i-1} e^{-\theta_i \Gamma_1}, \quad (3)$$

where k_i is the shape parameter, θ_i is the scale parameter, and $\Gamma(k)$ is the gamma function [for all positive integers $\Gamma(k) = (k-1)!$]. An example of a gamma-distributed prior with $k_i = 5$ is shown in Fig. 1(e) (black dashed line). A gamma-distributed prior yields a posterior that remains exactly gamma-distributed in the absence of state-preparation and measurement errors ($\alpha = \beta = 0$) when $m = 1$. Therefore, we expect that the posterior [see solid lines in Fig.1(e)] obtained via Eq. (2) using the prior in Eq. (3) is in all relevant cases still approximately gamma-distributed. The gamma distribution is also a convenient choice for the case when the standard deviation becomes comparable to the mean, since by definition it has zero weight at negative Γ_1 . For standard deviations small compared to the mean ($k_i \gg 1$) the gamma distribution approaches a Gaussian distribution.

In the following we will thus always approximate the probability distribution for Γ_1 after the i^{th} probing cycle with the gamma distribution $\mathcal{P}_i(\Gamma_1|k_i, \theta_i)$. We emphasize that while the gamma distribution is often associated with stochastic waiting times, in this work it is not linked to the physical origin of Γ_1 [48]. Rather, it is implemented in the controller for its mathematical convenience and since it provides a good approximation of a Gaussian distribution after sufficiently many measurements. In summary, the use of gamma distributions is advantageous as it requires two parameters (k_i, θ_i) only, and once multiplied by the exponential likelihood function (2), the posterior remains close to a gamma distribution. The controller thus only needs to keep track of two parameters after each measurement, which reduces the time the Bayesian update takes to $\approx 2.2 \mu\text{s}$, as mentioned above.

Two steps are required to implement the estimation in the controller. The first step is to determine an adaptive waiting time τ based on the prior distribution. Then, one must approximate the resulting posterior $\mathcal{P}_{i+1}(\Gamma_1)$ to a

gamma distribution. This can be done using equations implemented directly on the controller in real time.

a. Adaptive waiting time. Working within a Bayesian framework, a common approach is to choose parameters that minimize the expected value of a quantity that measures the inaccuracy of the Γ_1 estimate, such as the variance or Shannon information of its probability distribution, after a future measurement is obtained. This works well as long as one can find an analytical expression for the optimal experiment based on the chosen metric [49]. Here it turns out that even a simple metric like the expected posterior variance does not give a simple analytical update rule for choosing τ . Therefore, in our Bayesian framework, we make a similar heuristic choice for the adaptive parameter τ as in Ref. [34]: In each cycle, the controller uses the current estimate $\hat{T}_1 \equiv 1/\langle \Gamma_1 \rangle = \theta/k$ based on the prior distribution and uses the adaptive waiting time:

$$\tau_{i+1} = c \hat{T}_{1,i}, \quad (4)$$

where c is fixed in each experiment and depends on the qubit cycle idle time t (e.g., initialization, readout), and measurement error rates α and β . The optimal choice for the coefficient c is theoretically bound to the interval $c \in (0, 1.59)$ and is chosen based on binomial statistics, to reduce the estimation time locally and uncertainty given the current knowledge of Γ_1 (see the Supplemental Material [44]).

b. Posterior approximation. The prior $\mathcal{P}_i(\Gamma_1)$ in Eq. (2) is assumed to be a gamma distribution as given by Eq. (3), illustrated by the black dashed line in Fig. 1(e). After measuring $m_{i+1} = \{0, 1\}$, the posterior distribution $\mathcal{P}_{i+1}(\Gamma_1)$ is obtained by inserting Eqs. (1, 3) in Eq. (2). Since the posterior distribution is usually not an exact gamma distribution, we use the method of moments and approximate $\mathcal{P}_{i+1}(\Gamma_1)$ with the gamma distribution which has the same mean $\mu_{i+1} = E[\Gamma_1|m_{i+1}, \nu_{i+1}]$ and variance $\sigma_{i+1}^2 = E[\Gamma_1^2|m_{i+1}, \nu_{i+1}] - E[\Gamma_1|m_{i+1}, \nu_{i+1}]^2$ computed over $\mathcal{P}_{i+1}(\Gamma_1)$, where we use the notation $\nu_i \equiv (k_i, \theta_i, \tau_{i+1})$ [50]. The required gamma distribution then has the parameters

$$\theta_{i+1}^{-1} = f_m(k_i + 1, \theta_i, \tau_{i+1}) - f_m(k_i, \theta_i, \tau_{i+1}), \quad (5a)$$

$$k_{i+1}^{-1} = \frac{f_m(k_i + 1, \theta_i, \tau_{i+1})}{f_m(k_i, \theta_i, \tau_{i+1})} - 1, \quad (5b)$$

where

$$f_0(k, \theta, \tau) = \frac{k}{\theta} \frac{1 - \beta - (1 - \alpha - \beta) \left(\frac{\theta}{\theta + \tau}\right)^{k+1}}{1 - \beta - (1 - \alpha - \beta) \left(\frac{\theta}{\theta + \tau}\right)^k}, \quad (6a)$$

$$f_1(k, \theta, \tau) = \frac{k}{\theta} \frac{\beta + (1 - \alpha - \beta) \left(\frac{\theta}{\theta + \tau}\right)^{k+1}}{\beta + (1 - \alpha - \beta) \left(\frac{\theta}{\theta + \tau}\right)^k}. \quad (6b)$$

The approximated $\mathcal{P}_{i+1}(\Gamma_1)$ becomes then the new prior and the controller repeats this scheme in total N times

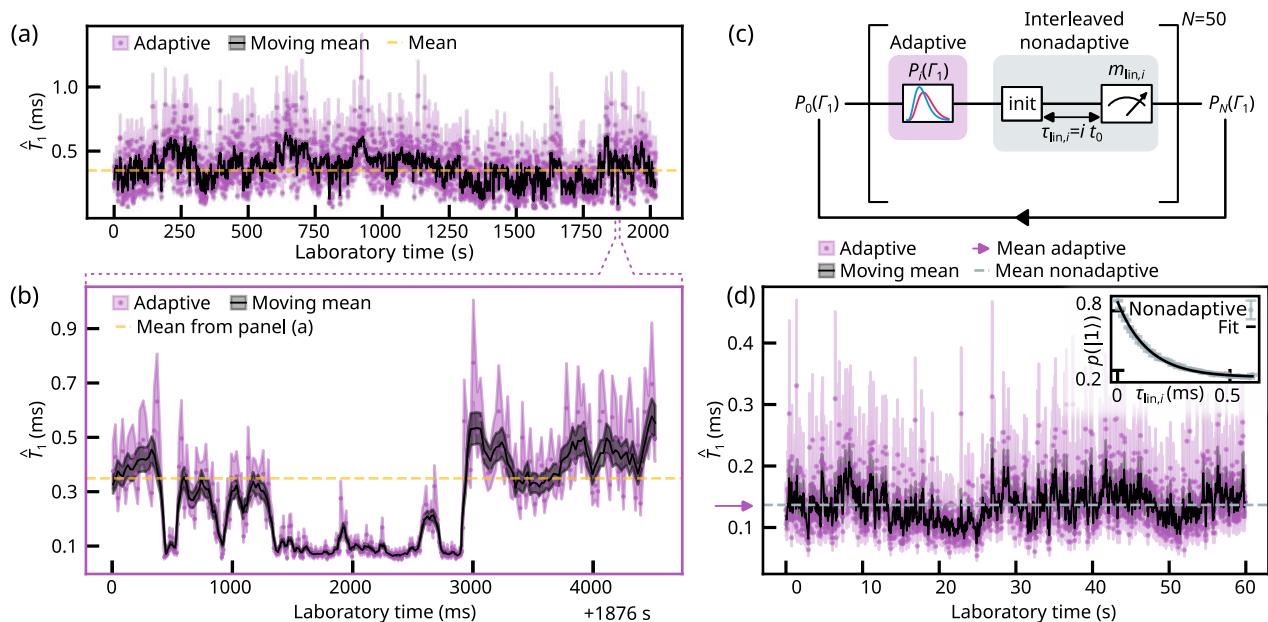


FIG. 2. **Protocol for tracking and validation of the decay-rate fluctuations by adaptive estimation on the controller.** (a) Experimental results for the adaptive tracking protocol with $N = 100$ to estimate \hat{T}_1 (purple dots, downsampled by $D = 30$) and its 68% credible interval (shaded area). Each purple point in this plot required an average estimation time of ≈ 20 ms. The dashed yellow line indicates the mean value of all estimates $\bar{T}_1 \approx 350 \mu\text{s}$. The black line is a moving mean over 100 samples and the black shaded area is its 68% confidence interval (see main text). (b) Estimated \hat{T}_1 at ≈ 1876 s of panel (a) (see purple dashed lines), where \hat{T}_1 shows telegraphic switching with timescales on the order of tens or hundreds of milliseconds. (c) The interleaved estimation sequence for Γ_1 used to validate the adaptive protocol. Each of the N probe cycles, labeled i , consists of parts contributing to the adaptive (purple) and nonadaptive (gray) estimates. Each adaptive probe cycle is followed by the nonadaptive part of the cycle, where the qubit is again initialized in the excited state, the wait time is fixed to $\tau_{\text{in},i} = i\tau_0$, and the measurement outcome is stored for offline post-processing. After the N probe cycles, the final adaptively obtained distribution $\mathcal{P}_N(\Gamma_1)$ is saved. (d) Experimental results for the adaptive tracking protocol, interleaved with nonadaptive measurements. Main panel: The estimate \hat{T}_1 (purple dots) and 68% credible interval (shaded area) corresponding to the final probability distribution $\mathcal{P}_{50}(\Gamma_1)$ of the 2,000 adaptive estimates performed during the ≈ 60 s of the experiment. The black line shows a moving mean over 5 samples and the black shaded area is its 68% confidence interval. The purple arrow indicates the mean of all the adaptive estimates \hat{T}_1 . The dashed line is the value extracted from the fit shown in the inset. Inset: Experimental results for the nonadaptive estimate using linearly sampled waiting time $\tau_{\text{in},i}$. Error bars represent the standard error.

per estimation repetition to obtain a sufficiently narrow distribution [51], during which Γ_1 is assumed to be quasistatic. If one were to relax the quasistatic approximation, the optimum choice of N would depend on details of the Γ_1 drift and the estimation efficiency [44, 52].

In Fig. 1(f) we illustrate (i) the resulting evolution of $\mathcal{P}_i(\Gamma_1)$ as a function of the measurement number i for one representative estimation sequence, and (ii) the corresponding waiting times τ_i and measurement outcomes m_i . The misclassification probabilities $\alpha = 0.11$ and $\beta = 0.14$ are obtained by fitting an exponential decay from the nonadaptive method (e.g. see inset of Fig. 2(d) and Fig. S3(c) of the Supplemental Material [44]). The initial prior is defined by $(k_0, \theta_0) = (3, 450 \mu\text{s})$, with $N = 50$ and $\tau \approx 0.51/\langle\Gamma_1\rangle$ [53], based on previously measured relaxation rate fluctuations. The purple line shows the estimates \hat{T}_1 and the shaded area indicates their 90% credible interval, narrowing \hat{T}_1 down from $168 \mu\text{s}$ (90% CI: $[80, 630] \mu\text{s}$) to

$191 \mu\text{s}$ (90% CI: $[133, 301] \mu\text{s}$) after 50 single-shot measurements. The user can pre-define the number of single-shot measurements based on the required target uncertainty, which is traded off against estimation speed. Upon measuring $m_i = 1$ (blue circle), the estimate $\hat{T}_{1,i}$ increases compared to its previous value, and the subsequent waiting time τ_{i+1} also increases. In contrast, after measuring $m_i = 0$ (red circle), $\hat{T}_{1,i}$ decreases, while τ_{i+1} decreases on average.

IV. RESULTS

A. Tracking high-frequency fluctuations by adaptive estimation

We now apply our fast adaptive method to characterize the qubit at a previously unexplored temporal resolution. We first task the controller to acquire a time

trace of \hat{T}_1 by the adaptive estimation, with $N = 100$ probe cycles [54] for each estimation repetition. We plot the estimated \hat{T}_1 on the controller in Fig. 2(a). The 68% confidence interval of the moving mean is computed using the standard error of the standard deviations of the 5 Bayesian posterior distributions: The standard error is estimated by first calculating the moving mean of the posterior standard deviations and then dividing by the square root of the window size. The confidence bounds are then determined as the moving mean of the estimated \hat{T}_1 values ± 1 standard error under normality assumption.

In Fig. 2(b), we plot the estimated \hat{T}_1 around 1878s of panel (a) (other windows are presented in the Supplemental Material [44]). As shown, \hat{T}_1 switches between $\approx 500 \mu\text{s}$ and $\approx 100 \mu\text{s}$ on a timescale of tens to hundreds of milliseconds. We emphasize that the purple points are *independent* of each other since at the beginning of each estimation repetition the prior distribution is reset to $\mathcal{P}_0(T_1)$.

The fluctuations in panels Fig. 2(a-b) exhibit telegraphic noise with multiple stable points, which could be explained by the qubit interacting with an ensemble of TLSs [14, 15, 24] changing due to spectral diffusion [22, 26] or background ionizing radiation [19]. We highlight that such fast fluctuations would not be measurable using the standard nonadaptive method, which has previously reported sampling times of a few seconds [18, 26, 27]. The dwell times, on the order of tens of milliseconds, are consistent with the state-switching dynamics observed in a TLS strongly coupled to a superconducting qubit used as a detector [55]. Our sampling interval, which is two orders of magnitude faster than previous works [18, 26, 27], reveals that significant T_1 fluctuations can occur at least one order of magnitude faster than previously reported in transmon qubits [18, 26–29].

The estimation time is only tens of times longer than the average T_1 and can be integrated into adaptive quantum control strategies to error-mitigate the performance of QPUs. One may imagine interleaving the estimation protocol with quantum circuit operations, executing them only when the estimated qubit relaxation time T_1 exceeds a user-defined threshold to maintain a target gate fidelity. Since T_1 fluctuates over time, instead of running quantum circuits continuously, the system can pause its execution when the relaxation rate is too high, thus improving the overall QPU fidelity. Since both the interleaved estimation and qubit operations are performed on the same qubit, there exists a nontrivial relationship between the correlation time of the fluctuations being tracked, the efficiency of the estimation process, and the duration required for coherent operations between estimations. Overall, the results presented in this section demonstrate that our Bayesian estimation protocol performs real-time tracking of the decay rate of a superconducting qubit.

B. Protocol validation by interleaved adaptive and nonadaptive estimations

Next, we validate the protocol by programming the controller to perform interleaved measurements with the nonadaptive method to verify that it correctly identifies the decay rate T_1 . The fluctuating parameter T_1 is estimated from the probing sequence shown in Fig. 2(c), where each probe cycle i begins with an adaptive cycle [see Fig. 1(b)] and is interleaved cycle-by-cycle with the nonadaptive one (gray) [56], the outcomes $m_{\text{lin},i}$ of which are stored.

In Fig. 2(d) we characterize the experimentally found final posterior probability distribution $\mathcal{P}_{50}(T_1)$ from 2,000 subsequent adaptive estimations. The 68% confidence interval of the moving mean is computed as in Fig. 2(a). In post-processing we calculate the 50 averages $\langle m_{\text{lin},i} \rangle$ and fit them to an exponentially decaying curve, see the inset panel of Fig. 2(d), which yields $T_1 = (136.7 \pm 2.2) \mu\text{s}$ (dashed gray line in the main panel). The 2,000 adaptive estimations give on average $\bar{T}_1 = (135.0 \pm 0.9) \mu\text{s}$ (purple arrow in the main panel), computed from the mean and standard error of the adaptive time trace shown in the main panel of Fig. 2(d). The main result is that the two values agree, and the reduced uncertainty of the adaptive method results from the narrowing of the prior distribution and the adaptive waiting time chosen for the experiment.

The controller performs the same interleaved estimation procedure on another qubit for over 3 minutes (Q_2 , located on the same chip, see the Supplemental Material [44]). In that case, the nonadaptive method yields $T_1 = (178.0 \pm 1.7) \mu\text{s}$, which is again in good agreement with the mean adaptive estimate $\bar{T}_1 = (182.63 \pm 0.55) \mu\text{s}$. Compared to Q_1 , we attribute the slightly larger discrepancy between these values to residual T_1 fluctuations occurring between the interleaved probing cycles.

C. Power spectral density and Allan deviation

To gain further insight into the physics of the fast fluctuations we observe, we calculate the power spectral density (PSD) and the Allan deviation [29, 41, 57] of a time trace of \hat{T}_1 acquired over 72 hours. The entire trace consists of $\approx 3.82 \times 10^7$ samples in total and is shown in Fig. 3(a). The controller uses $N = 49$ single-shot measurements per estimation repetition, with settings similar to those in Fig. 2(b) [58].

We compute the PSD [Fig. 3(b)] and Allan deviation [Fig. 3(c)] with a running 2.8-hour-long window (with 80% overlap) in the top panels and for the full trace in the lower panels. Compared to the controller's fast sampling period of ≈ 7 ms, the relatively long window enables us to resolve Lorentzian processes in the Allan deviation within hundreds of seconds of observation time. Later, in Fig. 4, we use narrower windows to highlight faster dynamics.

In Fig. 3(b), top panel, we show the power spectral

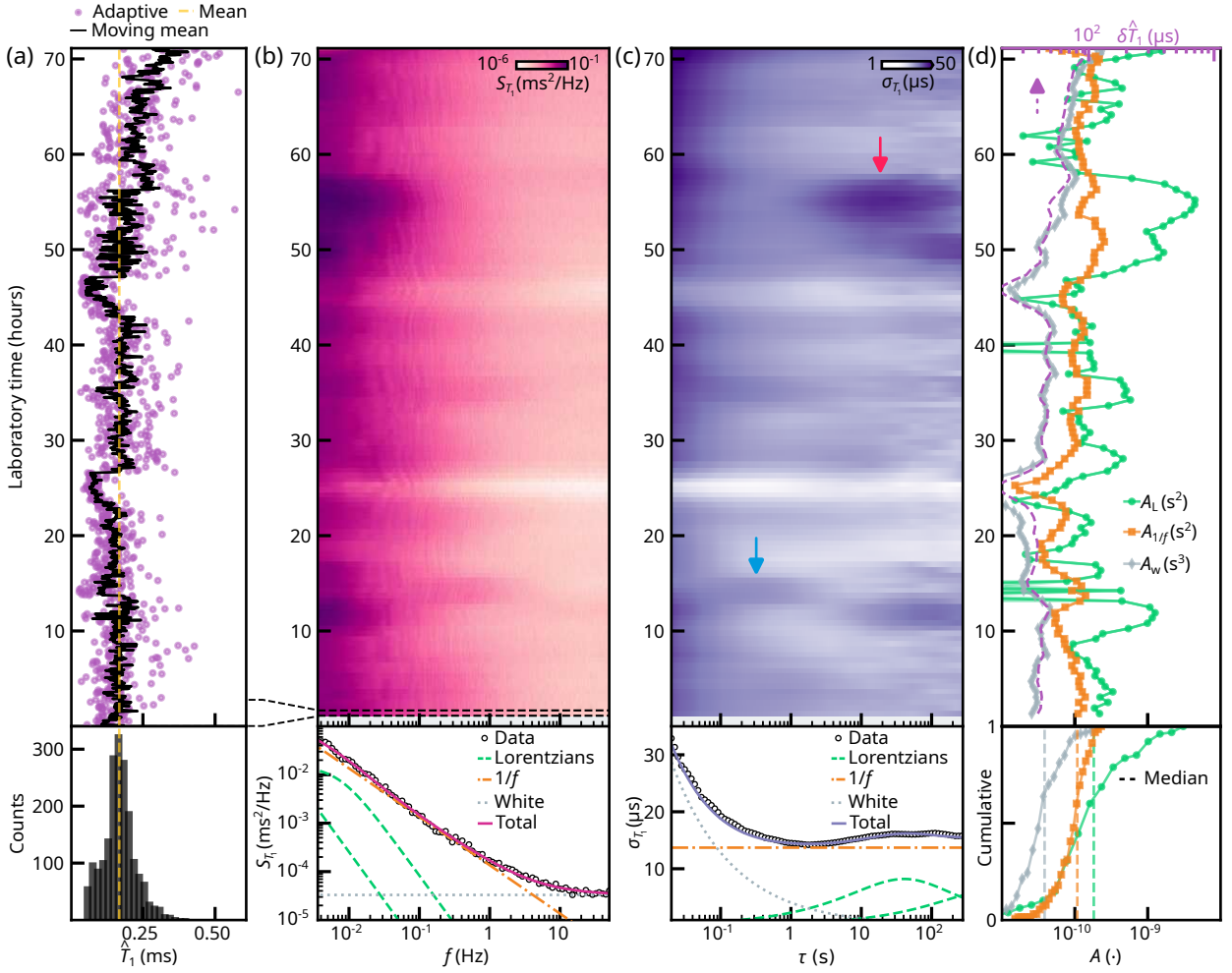


FIG. 3. **Frequency and time domain analysis of \hat{T}_1 fluctuations on a 72-hour timescale** (a) Estimated \hat{T}_1 (purple dots, downsampled by $D = 30,000$) as a function of laboratory time by real-time adaptive tracking with $N = 49$ and sampling speed of ≈ 7 ms over 72 hours. The dashed yellow line shows the mean value of all estimates $\bar{T}_1 \approx 168 \mu\text{s}$. The black line is a moving mean with a window of size 20,000 over the original estimates. Lower panel: Histogram of the moving mean. (b-c) Frequency and time domain analysis of the \hat{T}_1 fluctuations shown in panel (a), obtained from 2.8-hour running windows with 80% overlap (black dashed lines): (b) Power spectral density. Lower panel: PSD of the full time trace. (c) Allan deviation on a logarithmic scale; arrows denote the zoom-in regions of Fig. 4. Lower panel: Allan deviation of the full time trace. (d) Amplitudes of the Lorentzian (A_L), $1/f$ ($A_{1/f}$), and white noise (A_w) contributions, extracted from the full time trace, by a simultaneous PSD and Allan deviation fit to the analytical formulas from Table I. The purple dashed line is the standard deviation $\delta\hat{T}_1$ (see main text) of the Bayesian posterior distribution. Lower panel: Cumulative histogram of the fitted A_i and their medians (dashed lines).

density $S_{\hat{T}_1}(f)$. The PSD of $\hat{T}_1(t)$ is defined as the Fourier transform of its autocorrelation function:

$$S_{\hat{T}_1}(f) = \int_{-\infty}^{+\infty} \langle \hat{T}_1(t)\hat{T}_1(t+\tau) \rangle e^{-2\pi i f \tau} d\tau. \quad (7)$$

The PSD exhibits increased amplitude at low frequencies over some laboratory times, but attributing this behavior to a TLS is not straightforward, as even a few TLSs can produce a smooth, featureless $1/f$ spectrum that conceals individual contributions. In contrast, the Allan deviation quantifies how much a signal switches on average over an observation time τ . If an individual

TLS induces a random telegraph signal with a characteristic switching time, the Allan deviation of this signal exhibits a peak close to the average switching time of the TLS [29, 57].

For our qubit parameter $\hat{T}_1(t)$, the Allan deviation is defined as:

$$\sigma_{\hat{T}_1}(\tau) = \sqrt{\frac{1}{2} \langle (\bar{T}_1(t+\tau, \tau) - \bar{T}_1(t, \tau))^2 \rangle}, \quad (8)$$

where $\bar{T}_1(t, \tau) = \frac{1}{\tau} \int_t^{t+\tau} \hat{T}_1(t') dt'$ is the average over an interval of duration τ and $\langle \dots \rangle$ is the average over t . In Fig. 3(c), top panel, we plot $\sigma_{\hat{T}_1}(\tau)$ which is high at short

TABLE I. Power spectral density (PSD) and Allan deviation models for different noise processes. The amplitudes A_i and switching rate γ are free parameters for the simultaneous fit of the PSD and Allan deviation.

Noise	PSD $S_{\hat{T}_1}(f)$	Allan deviation $\sigma_{\hat{T}_1}(\tau)$
White	A_w	$\sqrt{A_w/\tau}$
$1/f$	$A_{1/f}f^{-1}$	$\sqrt{2A_{1/f}\ln 2}$
Lorentzian	$\frac{4A_L\gamma}{\gamma^2+(2\pi f)^2}$	$\sqrt{A_L\gamma\tau\sqrt{2\gamma\tau+1-(e^{-\gamma\tau}-2)^2}}$

observation times ($\tau \lesssim 100$ ms) due to high-frequency noise and sampling uncertainty. As τ increases, $\sigma_{\hat{T}_1}(\tau)$ decreases as the noise averages out. At longer τ , switching in \hat{T}_1 shows up as an increase in $\sigma_{\hat{T}_1}(\tau)$, which is clearly observed around τ in the range of tens of seconds at laboratory times of 11, 50, and 55 (red arrow) hours. Another striking feature is the peak at 14 hours (blue arrow) in the sub-second timescale. All the peaks shown in Fig. 3(c) are a clear signature of a Lorentzian noise process, as no power-law noise source can reproduce them, and they correspond to the rises in the PSD at smaller frequencies. The peaks of the Allan deviations are indications of individual TLSs that move in and out of resonance with the qubit [17, 18]. To our knowledge, these features have not been previously observed at such short observation timescales and are accessible here because of the fast and adaptive estimation protocol. The PSD and Allan deviation are lower at 25 and 45 hours of laboratory time, as a shorter T_1 generally corresponds to smaller fluctuations [26–29, 59, 60]. We tentatively attribute the shorter $\hat{T}_1 \approx 0.1$ ms to one or several TLSs being close to resonance with the qubit.

To quantify the impact of Lorentzian-type noise on the measured \hat{T}_1 fluctuations, it is common practice to fit the full time trace to a model including white noise, $1/f$ noise, and one or more Lorentzian noise sources [29]. We note that even if two Lorentzian processes fit the full trace, different TLS dynamics occur over laboratory time and it is actually sufficient for the fit to use only one Lorentzian in a shorter window slice. In the following, we present both analyses to support our claim.

In the bottom panels of Fig. 3(b-c) we plot the PSD and Allan deviation from the full trace shown in panel (a). Both curves are simultaneously fitted with a sum of white, $1/f$, and Lorentzian noise components, using the analytical expressions from Table I [29, 41]. Each noise process has a corresponding amplitude coefficient, A_i , which is a free parameter for the Allan deviation $\sigma_{\hat{T}_1}(\tau)$ and the power spectral density $S_{\hat{T}_1}(f)$ simultaneously. The Lorentzian fit also includes the switching rate γ as a free parameter. To fit the full trace we use two Lorentzian processes and the fit parameters are given by $A_w = (3.30 \pm 0.06) \times 10^{-5} \text{ s}^3$, $A_{1/f} = (1.36 \pm 0.02) \times 10^{-4} \text{ s}^2$, $A_{L,1} = (1.8 \pm 0.1) \times 10^{-4} \text{ s}^2$, $\gamma_1 = (46 \pm 5) \text{ mHz}$, $A_{L,2} = (1.0 \pm 0.3) \times 10^{-4} \text{ s}^2$, and

$$\gamma_2 = (2 \pm 1) \text{ mHz}.$$

Now, instead of the full trace, we fit each 2.8-hour-long time window of the top panels of Fig. 3(b-c) to show that only one Lorentzian process is sufficient to fit the data instead of two by selecting a shorter window. We plot the amplitudes of each noise process contribution in Fig. 3(d) and their cumulative histogram in the bottom panel. In the main panel of (d), the 68% confidence intervals of the fit parameters are smaller than the plotted symbols and are calculated as the square roots of the diagonal elements of the covariance matrix associated with the fit. The characteristic switching rate of the fitted Lorentzian component is shown in the Supplemental Material [44], including the close agreement between the model and the data. The $1/f$ noise likely originates from the qubit interacting with an ensemble of TLSs [14, 15, 24] which dominate the low-frequency fluctuations of T_1 as observed from our fit. The presence of distinct Lorentzian components supports the existence of a few strongly coupled fluctuators, consistent with the telegraphic switching observed in Fig. 2(b).

In Fig. 3(d) we also plot the standard deviation $\delta\hat{T}_1 \approx \langle \Gamma_1 \rangle^{-2} \delta\Gamma_1 = \theta k^{-3/2}$ (purple dashed line) from the posterior distribution computed on the controller. We note that $\delta\hat{T}_1$ correlates very well with A_w (gray diamonds), which is the fitted amplitude of the white noise contribution according to our model. The strong correlation between the white noise power and the posterior standard deviation suggests that $\delta\hat{T}_1$ indeed reflects the true uncertainty in the estimate. In other words, if the white noise scales with $\delta\hat{T}_1$ above a known noise floor, it is strong indirect evidence that the Bayesian posterior's $\delta\hat{T}_1$ reliably captures the actual estimation error. To our knowledge, such correlation in real-time estimation methods has not been reported before.

To quantitatively extract the occurrence rate of large telegraphic switches in \hat{T}_1 on tens of milliseconds timescales [Fig. 2(b)], we split the 72-hour-long time trace of Fig. 3(a) into independent 200-ms-long intervals. We find that $\approx 2.6\%$ of intervals exhibit on average changes in T_1 greater than $100 \mu\text{s}$, roughly one event every 7.7 s (see the Supplemental Material [44]).

As mentioned above, from Fig. 3(c) we observe dominant Lorentzian noise contributions for instance in the regions marked by the arrows. To highlight the fast noise dynamics pointed at by the blue arrow, we zoom in on the 2-hour time period around hour 14 and plot the \hat{T}_1 estimates in Fig. 4(a). To increase the temporal resolution, we analyze 7-minute intervals with 80% overlap and compute the corresponding Allan deviation for each, as shown in Fig. 4(b) with peaks around laboratory time of 14 hours and within sub-second observation time τ . The fitted parameters are presented in Fig. 4(c) alongside the switching rate γ in Fig. 4(d).

The fitted amplitudes reveal distinct periods during which Lorentzian fluctuators dominate the T_1 dynamics. In particular, the analysis identifies a more than one-hour-long window dominated by a single fluctuator with

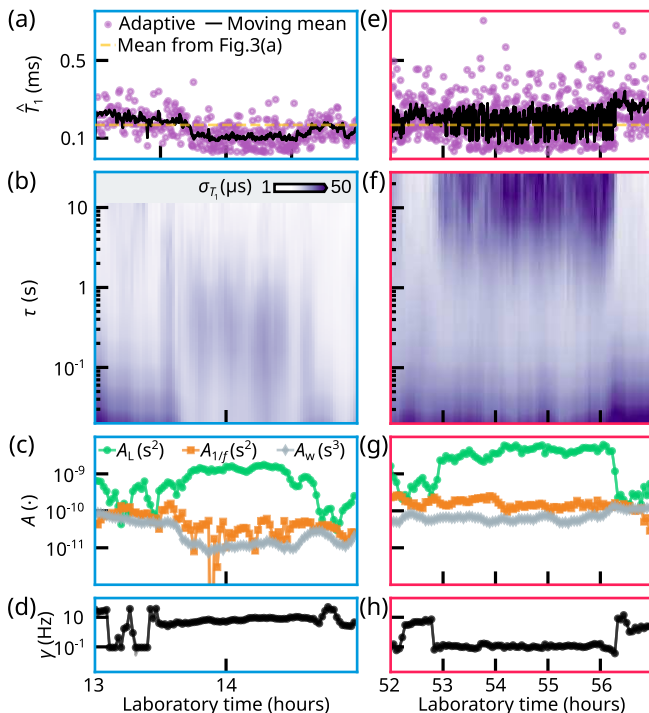


FIG. 4. **Time domain analysis of \hat{T}_1 fluctuations on sub-minute observation times.** Zoom-ins of the regions indicated by the arrows in Fig. 3(c). (a) Estimated \hat{T}_1 (purple dots, downsampled by $D = 3,000$) as a function of laboratory time. The dashed yellow line represents the mean value of all estimates \bar{T}_1 of Fig. 3(a). The black line is a moving mean with a window size of 3,000 over the original estimates. (b) Allan deviation in logarithmic scale of the \hat{T}_1 time trace with a running window of about 7 minutes and 80% overlap. (c) Amplitudes of the Lorentzian (A_L), $1/f$ ($A_{1/f}$), and white (A_w) noise contributions in each interval extracted from panel (a) by a simultaneous fit to the Allan deviation and PSD using analytical models from Table I. (d) Fitted switching rate $\gamma \approx 10$ Hz over more than one hour of the Lorentzian component. (e-h) Same as (a-d) with a running window of 17 minutes and 80% overlap. The switching rate fit in panel (h) reveals a stable Lorentzian process with $\gamma \approx 100$ mHz for more than 3 hours.

a relatively stable switching rate of $\gamma \approx 10$ Hz, consistent with the timescales observed by Ref. [55]. Such fast dynamics would be extremely challenging to probe with traditional nonadaptive methods.

We also focus on the region marked by the red arrow of Fig. 3(c) over 5 hours, see the corresponding \hat{T}_1 estimates in Fig. 4(e). Its Allan deviation is shown in Fig. 4(f), along with the fit parameters in panels (g) and (h). In this time span, the dominating TLS has a stable switching rate of about 100 mHz, slower than the 10 Hz presented in Fig. 4(d) but still two orders of magnitude faster than what is reported, for instance, in Ref. [29]. In panels (c, d, g, h), the 68% confidence intervals of the fit parameters are smaller than the plotted symbols and are calculated as in Fig. 3(d).

In this section we have demonstrated how our adaptive Bayesian estimation method, about two orders of magnitude faster than conventional nonadaptive methods [18, 26, 27], confirms dominant Lorentzian noise processes in transmon qubits in a previously unexplored regime of quickly fluctuating relaxation times.

V. CONCLUSIONS AND OUTLOOK

This work presents the experimental demonstration of an adaptive Bayesian estimation protocol for the decay rate of two fixed-frequency transmon qubits. The scheme probes sub-millisecond relaxation times using only tens of single-shot measurements, with total acquisition times of a few milliseconds. Our approach achieves rapid adaptive estimation of the decay rate by integrating real-time Bayesian estimation with FPGA-based feedback control. The protocol has been validated by interleaved measurements with the standard nonadaptive method of extracting the decay rate from fitting an exponential decay curve.

The main results of our work are (i) our fast protocol improves the state-of-the-art estimation speed by two orders of magnitude without compromising accuracy [18, 26, 27], (ii) it reveals clear telegraphic changes in T_1 by almost one order of magnitude [Fig. 2(b)], with dwell times of tens of milliseconds, instead of minutes or hours, most likely caused by interaction with an environmental bath of TLSs, and (iii) temporal and spectral analyses of the estimated fluctuations are consistent with dominant Lorentzian processes, from which switching rates as fast as 100 mHz and 10 Hz are resolved in Fig. 4, four orders of magnitude faster than previously reported. The estimation scheme is a powerful probe of dominant TLSs that switch in and out of resonance with the qubit on timescales of tens of seconds. Such timescales would be extremely difficult to observe with standard nonadaptive methods with the precision reported here, and they redefine the timescales relevant for calibration in superconducting QPUs, which traditionally operate on minute-to-hour cycles.

Our protocol uncovers new perspectives on materials characterization. High-throughput qubit screening targeting fast fluctuations previously required hours to accumulate sufficient statistics [16, 29]. While long acquisition times remain necessary for characterizing slow drifts, our scheme collects fast fluctuations statistics within seconds. Average relaxation times of $T_1 \gtrsim 100 \mu\text{s}$ [61, 62] have been shown in superconducting qubits, however achieving such results uniformly across a large wafer [10] and over time remains challenging. The overall performance is limited by the worst T_1 values, and T_1 tails can be improved through better fabrication that mitigates drops in T_1 . Our protocol provides a useful tool for qubit benchmarking and process control, enabling rapid optimization of superconducting qubits fabrication. Since the protocol employs only single-qubit gates, it can be read-

ily extended to multiple qubits simultaneously, and its adaptiveness makes it appealing for the characterization of large qubit arrays with unknown decay rates.

In future work, the protocol could be interleaved with dephasing rate measurements [27] using existing real-time estimation techniques [34, 40]. Potential correlations between decay and dephasing rates may provide insights into the microscopic origins of intrinsic decoherence channels at higher frequencies in Josephson junction qubits. Additionally, the estimation could be combined with spectral manipulation of TLSs via applied electric fields [21, 23, 62–64] or strain [63, 65]. Our adaptive Bayesian technique could be employed for simultaneous relaxation time estimations across multiple qubits [18, 60], to investigate temporal and spatial correlations at significantly higher frequency bandwidths than previously achieved. Spectral dynamics could also be explored in fixed-frequency transmons by implementing off-resonant microwave tones to drive AC Stark shifts [18, 23]. Additionally, our method could be applied for the rapid detection of qubit decay induced by gamma and cosmic rays [14, 15, 66, 67].

Potential modifications to the protocol include relaxing the assumption of single-shot readout [34], or mitigating state preparation and measurement errors by repeating probe cycles with the same waiting times [68, 69], at the cost of a slower estimation rate. Furthermore, the estimation could be optimized by terminating it once a target total measurement time or desired uncertainty is reached, rather than using a fixed number of single-shot measurements.

Fluctuations in the decay rate degrade the stability of QPUs, introduce uncertainty in coherence benchmarking, and hinder process optimization for superconducting qubits. Quantum error correction demonstrations are predominantly limited by the “worst” outlier qubits in a given processor [10, 12]. Since state-of-the-art gate fidelities are limited by T_1 , the optimal gate duration depends on temporal variations of T_1 . The observed stochastic decay rate fluctuations suggest the following error mitigation approach: Continuous identification of the lowest-performing qubits, suggesting a shift from offline periodic recalibration every few hours to real-time adaptive recalibration at millisecond timescales for maintaining higher-fidelity gate operations in QPUs. More generally, the ability to monitor a qubit’s relaxation rate in real time opens new opportunities for the dynamic optimization and routing of quantum algorithms. A recently estimated T_1 value could be passed to a compiler’s routing algorithm to determine the optimal mapping between virtual and physical qubits, thereby boosting the benchmarking or diagnostics of useful QPUs, and could be further extended to other platforms.

Our adaptive Bayesian technique also offers an efficient and online Hamiltonian learning protocol for real-time estimation of decay rates beyond superconducting qubits. Our results support that TLSs are major contributors to

rapid decay-rate fluctuations and a deeper understanding of TLSs is thus vital for further improving the performance of useful QPUs.

VI. ACKNOWLEDGMENTS

F.B., M.A.M., S.K., C.W.W., J.H. and M.K. gratefully acknowledge support from the Novo Nordisk Foundation (grant number NNF22SA0081175, the NNF Quantum Computing Programme), the Villum Foundation through a Villum Young Investigator grant (grant 37467), the European Union through an ERC Starting Grant (NovADePro, 101077479), the Innovation Fund Denmark (DanQ, Grant No. 2081-00013B), and the U.S. Army Research Office (Grant No. W911NF-22-1-0042). F.B., J. Benestad, J.A.K., J.D. and F.K. acknowledge funding from the European Union’s Horizon 2020 research and innovation programme under grant agreements 101017733 (QuantERA II), 101204890 (HORIZON-MSCA-2024-PF-01) and EUREKA Eurostars 3 (ECHIDNA), and from the Dutch National Growth Fund (NGF) as part of the Quantum Delta NL programme and the Research Council of Norway (RCN) under INTFELLES-Project No. 333990. O.K. received funding via the Innovation Fund Denmark for the project DIREC (9142-00001B). The device was fabricated at Myfab Chalmers. The Chalmers team was funded by the Knut and Alice Wallenberg Foundation through the Wallenberg Center for Quantum Technology (WACQT) and the EU Flagship on Quantum Technology HORIZON-CL4-2022-QUANTUM-01-SGA project 101113946 OpenSuperQPlus100. Any opinions, findings, conclusions, or recommendations expressed in this material are those of the author(s) and do not necessarily reflect the views of the Army Research Office, the US Government, the European Union, or the European Research Council. Neither the European Union nor the granting authority can be held responsible for them.

VII. AUTHOR CONTRIBUTIONS

F.B. led the measurements and data analysis, and wrote the manuscript with input from all authors. F.B., J. Benestad, J.H., F.K., M.K. performed the experiment with theoretical contributions from J.A.K., O.K., J.D. M.A.M. and S.K. developed experimental infrastructure. C.W.W. designed the device, which was fabricated by E.H., A.N., I.A., A.O., J. Biznárová, M.R. under the supervision of A.F.R., J. Bylander and G.T. The project was supervised by J.H., F.K. and M.K.

VIII. DATA AVAILABILITY

The data that support the findings of this article are openly available [70].

- [1] P. Krantz, M. Kjaergaard, F. Yan, T. P. Orlando, S. Gustavsson, and W. D. Oliver, A quantum engineer's guide to superconducting qubits, *Applied Physics Reviews* **6**, 021318 (2019).
- [2] H.-L. Huang, D. Wu, D. Fan, and X. Zhu, Superconducting quantum computing: a review, *Science China Information Sciences* **63**, 1 (2020).
- [3] A. Blais, A. L. Grimsmo, S. M. Girvin, and A. Wallraff, Circuit quantum electrodynamics, *Reviews of Modern Physics* **93**, 025005 (2021).
- [4] Y. Y. Gao, M. A. Rol, S. Touzard, and C. Wang, Practical guide for building superconducting quantum devices, *PRX Quantum* **2**, 040202 (2021).
- [5] S. E. Rasmussen, K. S. Christensen, S. P. Pedersen, L. B. Kristensen, T. Bækkegaard, N. J. S. Loft, and N. T. Zinner, Superconducting circuit companion—an introduction with worked examples, *PRX Quantum* **2**, 040204 (2021).
- [6] E. Campbell, A series of fast-paced advances in quantum error correction, *Nature Reviews Physics* **6**, 160 (2024).
- [7] L. Caune, L. Skoric, N. S. Blunt, A. Ruban, J. McDaniel, J. A. Valery, A. D. Patterson, A. V. Gramolin, J. Majaniemi, K. M. Barnes, T. Bialas, O. Buğdaycı, O. Crawford, G. P. Gehér, H. Krovi, *et al.*, Demonstrating real-time and low-latency quantum error correction with superconducting qubits [10.48550/arXiv.2410.05202](https://arxiv.org/abs/10.48550/arXiv.2410.05202) (2024).
- [8] Google Quantum AI and Collaborators, Quantum error correction below the surface code threshold, *Nature* **638**, 920 (2025).
- [9] I. Besedin, M. Kerschbaum, J. Knoll, I. Hesner, L. Bödeker, L. Colmenarez, L. Hofele, N. Lacroix, C. Hellings, F. Swiadek, A. Flasby, M. B. Panah, D. C. Zanuz, M. Müller, and A. Wallraff, Realizing lattice surgery on two distance-three repetition codes with superconducting qubits [10.48550/arXiv.2501.04612](https://arxiv.org/abs/10.48550/arXiv.2501.04612) (2025).
- [10] M. Mohseni, A. Scherer, K. G. Johnson, O. Wertheim, M. Otten, N. A. Aadit, K. M. Bresniker, K. Y. Camsari, B. Chapman, S. Chatterjee, G. A. Dagnew, A. Esposito, F. Fahim, M. Fiorentino, A. Khalid, *et al.*, How to build a quantum supercomputer: Scaling challenges and opportunities [10.48550/arXiv.2411.10406](https://arxiv.org/abs/10.48550/arXiv.2411.10406) (2024).
- [11] D. Gao, D. Fan, C. Zha, J. Bei, G. Cai, J. Cai, S. Cao, F. Chen, J. Chen, K. Chen, X. Chen, X. Chen, Z. Chen, Z. Chen, Z. Chen, *et al.*, Establishing a new benchmark in quantum computational advantage with 105-qubit Zhuchongzhi 3.0 processor, *Physical Review Letters* **134**, 090601 (2025).
- [12] Z. Wei, T. He, Y. Ye, D. Wu, Y. Zhang, Y. Zhao, W. Lin, H.-L. Huang, X. Zhu, and J.-W. Pan, Low-overhead defect-adaptive surface code with bandage-like super-stabilizers, *npj Quantum Information* **11**, 75 (2025).
- [13] P. J. J. O'Malley, J. Kelly, R. Barends, B. Campbell, Y. Chen, Z. Chen, B. Chiaro, A. Dunsworth, A. G. Fowler, I.-C. Hoi, E. Jeffrey, A. Megrant, J. Mutus, C. Neill, C. Quintana, *et al.*, Qubit metrology of ultralow phase noise using randomized benchmarking, *Physical Review Applied* **3**, 044009 (2015).
- [14] I. Siddiqi, Engineering high-coherence superconducting qubits, *Nature Reviews Materials* **6**, 875 (2021).
- [15] C. E. Murray, Material matters in superconducting qubits, *Materials Science and Engineering: R: Reports* **146**, 100646 (2021).
- [16] C. R. H. McRae, G. M. Stiehl, H. Wang, S.-X. Lin, S. A. Caldwell, D. P. Pappas, J. Mutus, and J. Combes, Reproducible coherence characterization of superconducting quantum devices, *Applied Physics Letters* **119**, 100501 (2021).
- [17] J. Béjanin, C. Earnest, A. Sharafeldin, and M. Mariantoni, Interacting defects generate stochastic fluctuations in superconducting qubits, *Physical Review B* **104**, 094106 (2021).
- [18] M. Carroll, S. Rosenblatt, P. Jurcevic, I. Lauer, and A. Kandala, Dynamics of superconducting qubit relaxation times, *npj Quantum Information* **8**, 132 (2022).
- [19] T. Thorbeck, A. Eddins, I. Lauer, D. T. McClure, and M. Carroll, Two-level-system dynamics in a superconducting qubit due to background ionizing radiation, *PRX Quantum* **4**, 020356 (2023).
- [20] D. Colao Zanuz, Q. Ficheux, L. Michaud, A. Orekhov, K. Hanke, A. Flasby, M. Bahrami Panah, G. J. Norris, M. Kerschbaum, A. Remm, F. Swiadek, C. Hellings, S. Lazăr, C. Scarato, N. Lacroix, *et al.*, Mitigating losses of superconducting qubits strongly coupled to defect modes, *Physical Review Applied* **23**, 044054 (2025).
- [21] Y. Kim, L. C. Govia, A. Dane, E. van den Berg, D. M. Zajac, B. Mitchell, Y. Liu, K. Balakrishnan, G. Keefe, A. Stabile, *et al.*, Error mitigation with stabilized noise in superconducting quantum processors, *Nature Communications* **16**, 8439 (2025).
- [22] S. Weeden, D. C. Harrison, S. Patel, M. Snyder, E. J. Blackwell, G. Spahn, S. Abdullah, Y. Takeda, B. L. T. Plourde, J. M. Martinis, and R. McDermott, Statistics of strongly coupled defects in superconducting qubits [10.48550/arXiv.2506.00193](https://arxiv.org/abs/10.48550/arXiv.2506.00193) (2025).
- [23] L. Chen, K.-H. Lee, C.-H. Liu, B. Marinelli, R. K. Naik, Z. Kang, N. Goss, H. Kim, D. I. Santiago, and I. Siddiqi, Scalable and site-specific frequency tuning of two-level system defects in superconducting qubit arrays [10.48550/arXiv.2503.04702](https://arxiv.org/abs/10.48550/arXiv.2503.04702) (2025).
- [24] C. Müller, J. H. Cole, and J. Lisenfeld, Towards understanding two-level-systems in amorphous solids: insights from quantum circuits, *Reports on Progress in Physics* **82**, 124501 (2019).
- [25] Y. Shalibo, Y. Rofe, D. Shwa, F. Zeides, M. Neeley, J. M. Martinis, and N. Katz, Lifetime and coherence of two-level defects in a Josephson junction, *Physical Review Letters* **105**, 177001 (2010).
- [26] P. V. Klimov, J. Kelly, Z. Chen, M. Neeley, A. Megrant, B. Burkett, R. Barends, K. Arya, B. Chiaro, Y. Chen, A. Dunsworth, A. Fowler, B. Foxen, C. Gidney, M. Giustina, R. Graff, *et al.*, Fluctuations of energy-relaxation times in superconducting qubits, *Physical Review Letters* **121**, 090502 (2018).
- [27] S. Schlör, J. Lisenfeld, C. Müller, A. Bilmes, A. Schneider, D. P. Pappas, A. V. Ustinov, and M. Weides, Correlating decoherence in transmon qubits: Low frequency noise by single fluctuators, *Physical Review Letters* **123**, 190502 (2019).
- [28] C. Müller, J. Lisenfeld, A. Shnirman, and S. Poletto, Interacting two-level defects as sources of fluctuating high-frequency noise in superconducting circuits, *Physical Review B* **92**, 035442 (2015).

- [29] J. J. Burnett, A. Bengtsson, M. Scigliuzzo, D. Niepce, M. Kudra, P. Delsing, and J. Bylander, Decoherence benchmarking of superconducting qubits, *npj Quantum Information* **5**, 132 (2019).
- [30] C. E. Granade, C. Ferrie, N. Wiebe, and D. G. Cory, Robust online Hamiltonian learning, *New Journal of Physics* **14**, 103013 (2012).
- [31] V. Gebhart, R. Santagati, A. A. Gentile, E. M. Gauger, D. Craig, N. Ares, L. Bianchi, F. Marquardt, L. Pezzè, and C. Bonato, Learning quantum systems, *Nature Reviews Physics* **5**, 141 (2023).
- [32] M. Spiecker, P. Paluch, N. Gosling, N. Drucker, S. Matityahu, D. Gusenkova, S. Günzler, D. Rieger, I. Takmakov, F. Valenti, *et al.*, Two-level system hyperpolarization using a quantum Szilard engine, *Nature Physics* **19**, 1320 (2023).
- [33] K. Reuer, J. Landgraf, T. Fösel, J. O’Sullivan, L. Beltrán, A. Akin, G. J. Norris, A. Remm, M. Kerschbaum, J.-C. Besse, *et al.*, Realizing a deep reinforcement learning agent for real-time quantum feedback, *Nature Communications* **14**, 7138 (2023).
- [34] M. J. Arshad, C. Bekker, B. Haylock, K. Skrzypczak, D. White, B. Griffiths, J. Gore, G. W. Morley, P. Salter, J. Smith, I. Zohar, A. Finkler, Y. Altmann, E. M. Gauger, and C. Bonato, Real-time adaptive estimation of decoherence timescales for a single qubit, *Physical Review Applied* **21**, 024026 (2024).
- [35] F. Berritta, T. Rasmussen, J. A. Krzywda, J. van der Heijden, F. Fedele, S. Fallahi, G. C. Gardner, M. J. Manfra, E. van Nieuwenburg, J. Danon, A. Chatterjee, and F. Kuemmeth, Real-time two-axis control of a spin qubit, *Nature Communications* **15**, 1676 (2024).
- [36] N. Dumoulin Stuyck, A. E. Seedhouse, S. Serrano, T. Tanttu, W. Gilbert, J. Y. Huang, F. Hudson, K. M. Itoh, A. Laucht, W. H. Lim, C. H. Yang, A. Saraiva, and A. S. Dzurak, Silicon spin qubit noise characterization using real-time feedback protocols and wavelet analysis, *Applied Physics Letters* **124**, 114003 (2024).
- [37] N. R. Vora, Y. Xu, A. Hashim, N. Fruitwala, H. N. Nguyen, H. Liao, J. Balewski, A. Rajagopala, K. Nowrouzi, Q. Ji, *et al.*, ML-powered FPGA-based real-time quantum state discrimination enabling mid-circuit measurements [10.48550/arXiv.2406.18807](https://arxiv.org/abs/10.48550/arXiv.2406.18807) (2024).
- [38] F. Berritta, J. A. Krzywda, J. Benestad, J. van der Heijden, F. Fedele, S. Fallahi, G. C. Gardner, M. J. Manfra, E. van Nieuwenburg, J. Danon, A. Chatterjee, and F. Kuemmeth, Physics-informed tracking of qubit fluctuations, *Physical Review Applied* **22**, 014033 (2024).
- [39] J. Park, H. Jang, H. Sohn, J. Yun, Y. Song, B. Kang, L. E. A. Stehouwer, D. D. Esposti, G. Scappucci, and D. Kim, Passive and active suppression of transduced noise in silicon spin qubits, *Nature Communications* **16**, 78 (2025).
- [40] F. Berritta, J. Benestad, L. Pahl, M. Mathews, J. A. Krzywda, R. Assouly, Y. Sung, D. K. Kim, B. M. Niedzielski, K. Serniak, M. E. Schwartz, J. L. Yoder, A. Chatterjee, J. A. Grover, J. Danon, W. D. Oliver, and F. Kuemmeth, Efficient qubit calibration by binary-search Hamiltonian tracking, *PRX Quantum* **6**, 030335 (2025).
- [41] C. M. Van Vliet and P. H. Handel, A new transform theorem for stochastic processes with special application to counting statistics, *Physica A: Statistical Mechanics and its Applications* **113**, 261 (1982).
- [42] R. C. Kurchin, Using Bayesian parameter estimation to learn more from data without black boxes, *Nature Reviews Physics* **6**, 152 (2024).
- [43] C. W. Warren, J. Fernández-Pendás, S. Ahmed, T. Abad, A. Bengtsson, J. Biznárová, K. Debnath, X. Gu, C. Krizan, A. Osman, A. Fadavi Roudsari, P. Delsing, G. Johansson, A. Frisk Kockum, G. Tancredi, and J. Bylander, Extensive characterization and implementation of a family of three-qubit gates at the coherence limit, *npj Quantum Information* **9**, 44 (2023).
- [44] See the Supplemental Material at URL for the experimental setup, additional examples of decay-rate estimation for both qubits, and theoretical details on the optimal waiting time based on binomial statistics and on the decay-rate estimation using gamma distributions. The Supplemental Material includes Refs. [71, 72].
- [45] D. Ristè, C. Bultink, K. W. Lehnert, and L. DiCarlo, Feedback control of a solid-state qubit using high-fidelity projective measurement, *Physical Review Letters* **109**, 240502 (2012).
- [46] Our model assumes that an exponential decay well approximates a relaxation time experiment. However, this assumption breaks down in the presence of strong coupling between the qubit and a TLS, which induces oscillations in the excited-state return probability. If the oscillation frequency is known, the protocol can be easily adapted by sampling at the maxima (or minima) of these oscillations. Otherwise, the model must be extended for multi-parameter Bayesian estimation [34, 73]. Such strong coupling regimes have not been observed in Q_1 and Q_2 during our experiments.
- [47] C. Ferrie, C. E. Granade, and D. G. Cory, How to best sample a periodic probability distribution, or on the accuracy of Hamiltonian finding strategies, *Quantum Information Processing* **12**, 611 (2013).
- [48] A gamma distribution models the statistics of the sum of independent decay processes, where the random variable represents the total decay time. In that sense, it is naturally related to decay dynamics. However, in our case, we measure the state m rather than the actual decay time τ . As a result, the relevant statistics are binomial rather than the exponential distribution typically associated with lifetime studies. Therefore, the appearance of the gamma distribution in this work is not due to physical origins, but rather because it closely resembles the true posterior.
- [49] Thus for adaptive methods, the Shannon information is rarely used in practice, as it tends to be computationally intractable.
- [50] For $(\alpha = \beta = 0)$, we have $E[\Gamma_1 | m_i, \nu_i] = k/\theta$ and $E[\Gamma_1^2 | m_i, \nu_i] = (k_i + k_i^2)/\theta_i^2$ (see the Supplemental Material [44] for the case $\alpha, \beta \neq 0$).
- [51] We perform a numerical approximation of the Kullback–Leibler divergence (D_{KL}) to estimate how much the posterior distribution differs from our gamma-distribution approximation. The largest deviation occurs for the worst-case outcome $m = 1$ together with a small prior shape parameter, typically $k = 3$. In this regime the posterior is strongly skewed, and the approximation error reaches a maximum of roughly $D_{KL} \approx 0.09$ – 0.10 at intermediate ratios $\tau_{i+1}/\theta \gtrsim 1$. The accuracy improves systematically with increasing k . For example, at $k = 10$ the peak divergence drops below 0.006, and for $k = 20$ it falls below 0.001 across the entire range of τ_{i+1}/θ . See the

- Supplemental Material [44] for further details on the validity of the approximation, also with respect to a normal distribution.
- [52] J. Benestad, J. Krzywda, E. van Nieuwenburg, and J. Danon, Efficient adaptive Bayesian estimation of a slowly fluctuating overhauser field gradient, *SciPost Physics* **17**, 014 (2024).
- [53] Due to the numerical precision of the controller, the actual ratio between τ_{i+1} and $\hat{T}_{1,i}$ varies by approximately 10% in the vast majority of probe cycles.
- [54] Each probe cycle includes a 2.5 μs readout period, followed by an approximately 8 μs wait time to allow the resonator to cool down and fully deplete any residual photons from the readout pulse. Each Bayesian update takes $\approx 2.2 \mu\text{s}$. The controller is programmed to start with an initial gamma distribution prior with $(k_0, \theta_0) = (3, 450 \mu\text{s})$. With this in mind, the adaptive waiting time in each cycle is set to $\tau_{i+1} \approx 0.51 \hat{T}_{1,i}$ (see the Supplemental Material [44] for a motivation of the choice $c = 0.51$), where $\hat{T}_{1,i}$ is the estimator for T_1 after cycle i .
- [55] S. M. Meißner, A. Seiler, J. Lisenfeld, A. V. Ustinov, and G. Weiss, Probing individual tunneling fluctuators with coherently controlled tunneling systems, *Physical Review B* **97**, 180505 (2018).
- [56] Here $(k_0, \theta_0) = (3, 450 \mu\text{s})$, $\alpha = 0.11$, $\beta = 0.14$. Considering also that the nonadaptive $\tau_{\text{in},i}$ is linearly stepped up to $\approx 600 \mu\text{s}$, the average idle time from the point of view of the adaptive scheme is $t \approx 345 \mu\text{s}$, mostly covered by the average $\langle \tau_{\text{in},i} \rangle \approx 300 \mu\text{s}$. The adaptive waiting time in each cycle is then set to $\tau_{i+1} \approx 0.98 \hat{T}_{1,i}$ (see the Supplemental Material [44]).
- [57] F. Ye, A. Ellaboudy, D. Albrecht, R. Vudatha, N. T. Jacobson, and J. M. Nichol, Characterization of individual charge fluctuators in Si/SiGe quantum dots, *Physical Review B* **110**, 235305 (2024).
- [58] $(k_0, \theta_0) = (3, 600 \mu\text{s})$, $\alpha = \beta = 0.12$, and $c \approx 0.53$.
- [59] M. Bal, A. A. Murthy, S. Zhu, F. Crisa, X. You, Z. Huang, T. Roy, J. Lee, D. v. Zanten, R. Pilipenko, *et al.*, Systematic improvements in transmon qubit coherence enabled by niobium surface encapsulation, *npj Quantum Information* **10**, 43 (2024).
- [60] S. Kono, J. Pan, M. Chegnizadeh, X. Wang, A. Youssefi, M. Scigliuzzo, and T. J. Kippenberg, Mechanically induced correlated errors on superconducting qubits with relaxation times exceeding 0.4 ms, *Nature Communications* **15**, 3950 (2024).
- [61] M. Tuokkola, Y. Sunada, H. Kivijärvi, J. Albanese, L. Grönberg, J.-P. Kaikkonen, V. Vesterinen, J. Govenius, and M. Möttönen, Methods to achieve near-millisecond energy relaxation and dephasing times for a superconducting transmon qubit, *Nature Communications* **16**, 5421 (2025).
- [62] A. Dane, K. Balakrishnan, B. Wacaser, L.-W. Hung, H. J. Mamin, D. Rugar, R. M. Shelby, C. Murray, K. Rodbell, and J. Sleight, Performance stabilization of high-coherence superconducting qubits [10.48550/arXiv.2503.12514](https://arxiv.org/abs/2503.12514) (2025).
- [63] J. Lisenfeld, A. Bilmes, A. Megrant, R. Barends, J. Kelly, P. Klimov, G. Weiss, J. M. Martinis, and A. V. Ustinov, Electric field spectroscopy of material defects in transmon qubits, *npj Quantum Information* **5**, 105 (2019).
- [64] A. Bilmes, A. Megrant, P. Klimov, G. Weiss, J. M. Martinis, A. V. Ustinov, and J. Lisenfeld, Resolving the positions of defects in superconducting quantum bits, *Scientific reports* **10**, 3090 (2020).
- [65] G. J. Grabovskij, T. Peichl, J. Lisenfeld, G. Weiss, and A. V. Ustinov, Strain tuning of individual atomic tunneling systems detected by a superconducting qubit, *Science* **338**, 232 (2012).
- [66] J. M. Martinis, Saving superconducting quantum processors from decay and correlated errors generated by gamma and cosmic rays, *npj Quantum Information* **7**, 90 (2021).
- [67] P. M. Harrington, M. Li, M. Hays, W. Van De Pontseele, D. Mayer, H. D. Pinckney, F. Contipelli, M. Gingras, B. M. Niedzielski, H. Stickler, *et al.*, Synchronous detection of cosmic rays and correlated errors in superconducting qubit arrays, *Nature Communications* **16**, 6428 (2025).
- [68] A. Sergeevich, A. Chandran, J. Combes, S. D. Bartlett, and H. M. Wiseman, Characterization of a qubit Hamiltonian using adaptive measurements in a fixed basis, *Physical Review A* **84**, 052315 (2011).
- [69] P. Cappellaro, Spin-bath narrowing with adaptive parameter estimation, *Physical Review A* **85**, 030301 (2012).
- [70] F. Berritta, J. Benestad, J. Krzywda, O. Krause, M. A. M. Nielsen, S. Krøjer, C. Warren, E. Rehnman, A. Nylander, I. Ahmad, A. Osman, J. Biznárová, M. Rommel, A. Fadavi Roudsari, J. Bylander, G. Tancredi, J. Danon, J. Hastrup, F. Kuemmeth, and M. Kjaergaard, Dataset underlying the manuscript: Real-time adaptive tracking of fluctuating relaxation rates in superconducting qubits, [10.5281/zenodo.17345142](https://zenodo.org/record/17345142) (2026).
- [71] S. Gustavsson, F. Yan, G. Catelani, J. Bylander, A. Kamal, J. Birenbaum, D. Hover, D. Rosenberg, G. Samach, A. P. Sears, *et al.*, Suppressing relaxation in superconducting qubits by quasiparticle pumping, *Science* **354**, 1573 (2016).
- [72] F. Leveraro, *Novel techniques for fast and precise estimation of qubit decay rates*, Master's thesis, University of Copenhagen (2024).
- [73] M. Valeri, V. Cimini, S. Piacentini, F. Ceccarelli, E. Polino, F. Hoch, G. Bizzarri, G. Corrielli, N. Spagnolo, R. Osellame, *et al.*, Experimental multiparameter quantum metrology in adaptive regime, *Physical Review Research* **5**, 013138 (2023).

Supplemental Material for “Real-time adaptive tracking of fluctuating relaxation rates in superconducting qubits”

Fabrizio Berritta,^{*} Malthe A. Marciniak, Svend Krøjer, Jacob Hastrup, and Morten Kjaergaard[†]
*Center for Quantum Devices, Niels Bohr Institute, University of Copenhagen, 2100 Copenhagen, Denmark and
NNF Quantum Computing Programme, Niels Bohr Institute, University of Copenhagen, 2100 Copenhagen, Denmark*

Jacob Benestad and Jeroen Danon
*Center for Quantum Spintronics, Department of Physics, Norwegian
University of Science and Technology, NO-7491 Trondheim, Norway*

Oswin Krause
Department of Computer Science, University of Copenhagen, 2100 Copenhagen, Denmark

Jan A. Krzywda
*Lorentz Institute for Theoretical Physics & Leiden Institute of Advanced Computer Science,
Universiteit Leiden, 2311 EZ Leiden, The Netherlands*

Christopher W. Warren
*Department of Microtechnology and Nanoscience, Chalmers University of Technology, SE-412 96 Gothenburg, Sweden
Center for Quantum Devices, Niels Bohr Institute, University of Copenhagen, 2100 Copenhagen, Denmark and
NNF Quantum Computing Programme, Niels Bohr Institute, University of Copenhagen, 2100 Copenhagen, Denmark*

Emil Hogedal, Andreas Nylander, Irshad Ahmad, Amr Osman, Janka Biznárová,
Marcus Rommel, Anita Fadavi Roudsari, Jonas Bylander, and Giovanna Tancredi
Department of Microtechnology and Nanoscience, Chalmers University of Technology, SE-412 96 Gothenburg, Sweden

Ferdinand Kuemmeth
*Center for Quantum Devices, Niels Bohr Institute, University of Copenhagen, 2100 Copenhagen, Denmark
Institute of Experimental and Applied Physics, University of Regensburg, 93040 Regensburg, Germany and
QDevil, Quantum Machines, 2750 Ballerup, Denmark*
(Dated: February 13, 2026)

CONTENTS

Experimental setup	2
Adaptive estimation in Q_1 : additional examples of fast fluctuations	4
Decay-rate estimation in Q_2	5
Adaptive estimation	5
Interleaved adaptive and nonadaptive estimations	6
Interleaved estimations with and without active reset	7
Optimal waiting time with binomial statistics	8
Adaptive waiting time implementation on the controller	9
Optimal waiting time with the number of measurements	9
Decay-rate estimation with gamma distributions	11
Comparison of nonadaptive and adaptive Bayesian methods	13
How SPAM affects the estimation protocol	13

Validity of the gamma approximation	14
Quasistatic approximation and Markovianity	16
Theoretical estimation uncertainty limit	17
Validation of Estimated values of T_1	18
Frequency of events of large switches in T_1	20
Fit to Allan Deviation and Power Spectral Density	21
References	22

EXPERIMENTAL SETUP

The measurements are performed in a Bluefors XLD400 dilution refrigerator with a base temperature below 10 mK and the setup is sketched in Fig. S1. The Quantum Machines OPX1000 is used for the XY control of the qubit and readout signal, and both microwave pulses are generated by direct digital synthesis. Each drive pulse is 60-ns long, with a Gaussian envelope of 12-ns standard deviation. The readout pulse is 2.5- μ s long, with a cosine rise and fall envelope of 20 ns each.

The OPX1000 includes real-time classical processing with fast analog feedback programmed in QUA software. The readout resonator linewidth $\kappa_r/(2\pi) \approx 110$ kHz, and the microwave readout tone, approximately 6.94 GHz, is filtered and attenuated at room temperature by passive components. The readout tone is attenuated in the cryostat to remove excess thermal photons from higher-temperature stages, and low-pass filtered at the mixing chamber. The device sample is wirebonded to the printed circuit board (PCB) of a QCage.24 sample holder and the chip is suspended by four corners inside a cavity and clamped down by the PCB. The sample holder is placed inside a light-tight superconducting aluminum enclosure to reject stray microwave and infrared photons and it is then shielded magnetically with a QCage Magnetic Shielding. Both the sample holder and the magnetic shield are supplied by Quantum Machines. The transmitted signal from the feedline goes to a high-electron-mobility transistor amplifier thermally anchored at the 3 K stage to amplify the readout signal further. At room temperature, the readout line is again amplified.

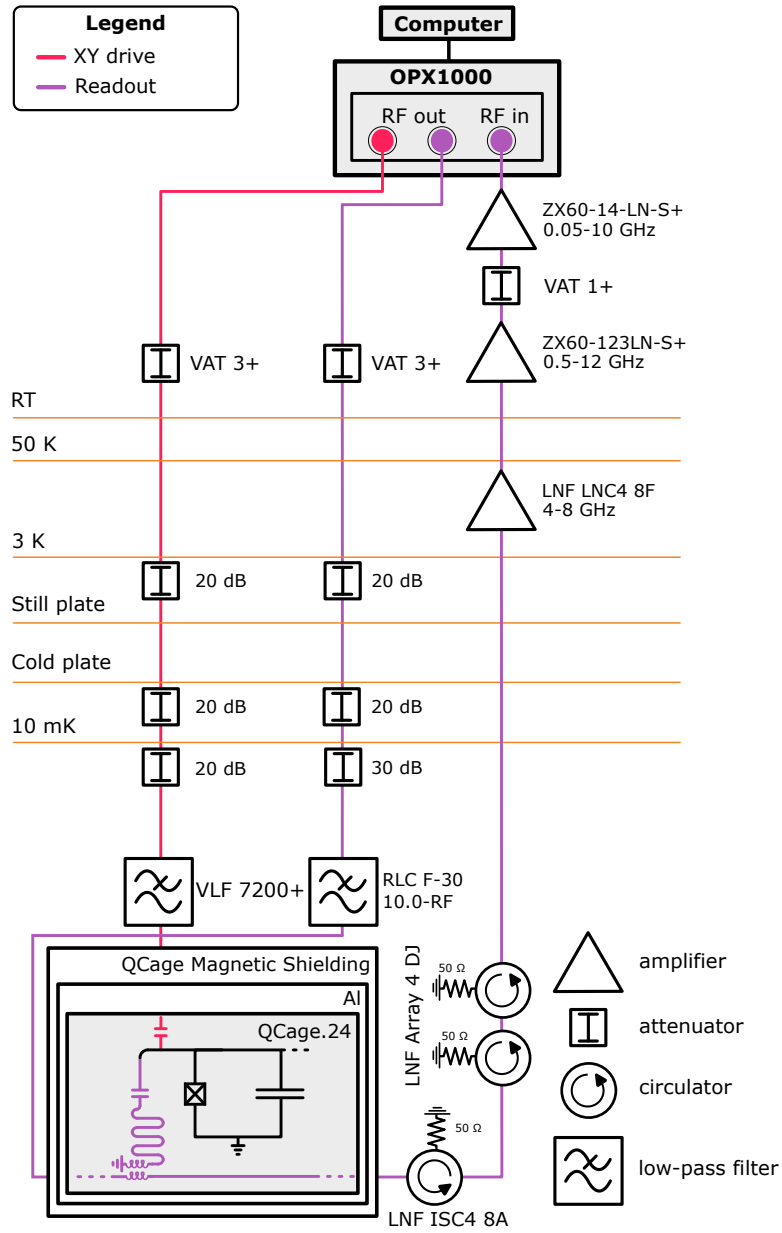


FIG. S1. **Experimental setup.** The cryostat is a Bluefors XLD400 dilution refrigerator with a base temperature lower than 10 mK. A Quantum Machines OPX1000 is used for the XY drive pulses and readout.

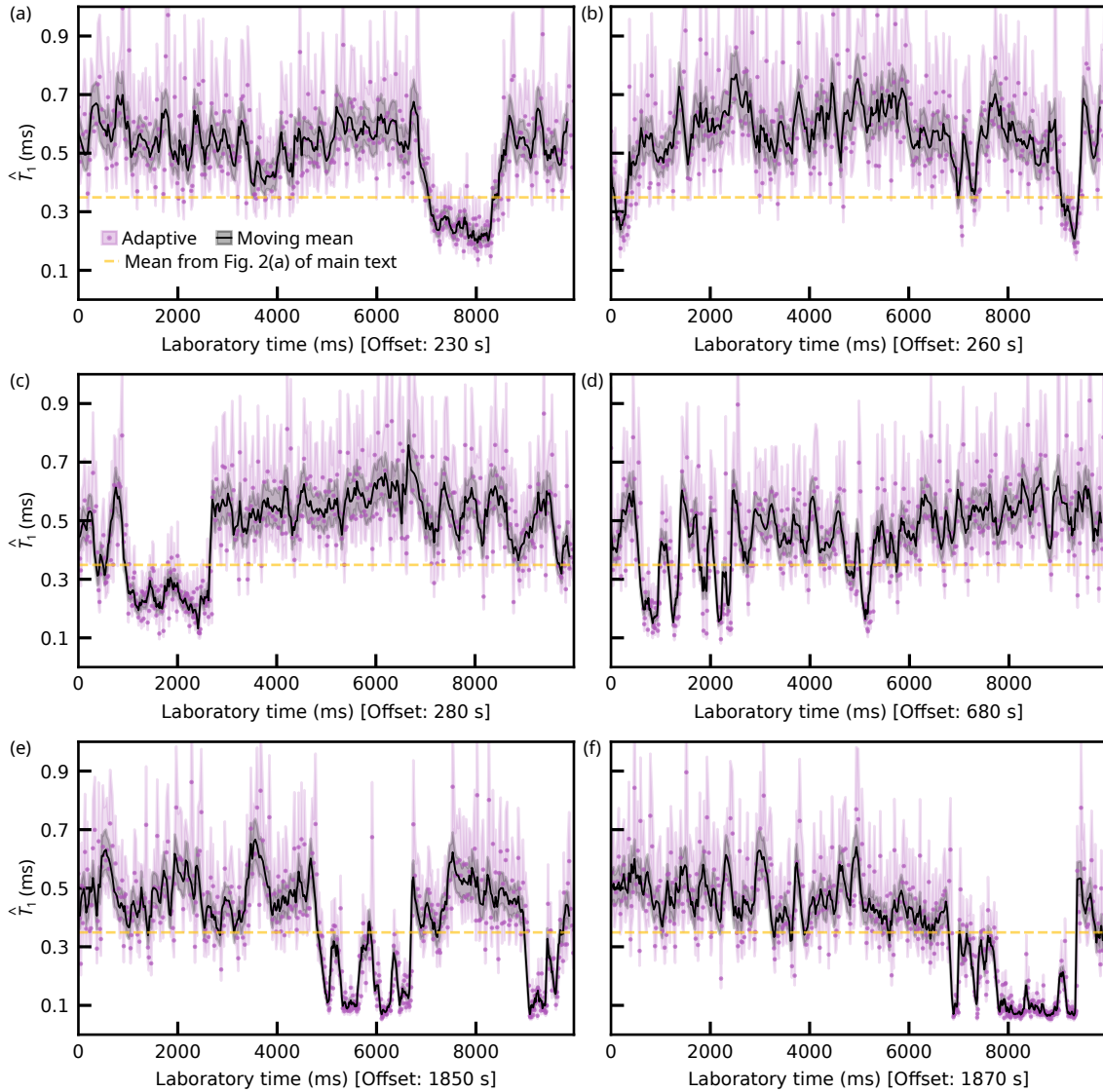


FIG. S2. **Tracking of the decay-rate fluctuations in Q_1 by adaptive estimation on the controller.** (a-f) Plotting not downsampled windows of Fig. 2(a) of the main text, where \hat{T}_1 shows fast switching with timescales on the order of tens or hundreds of milliseconds. Panel (f) includes Fig. 2(b) of the main text.

ADAPTIVE ESTIMATION IN Q_1 : ADDITIONAL EXAMPLES OF FAST FLUCTUATIONS

In Fig. S2 we plot different 10-second-long windows of the time trace shown in Fig. 2(a) of the main text. The fluctuations show telegraphic switching between high values of $\hat{T}_1 > 500 \mu\text{s}$ and low values $\hat{T}_1 \approx 100 \mu\text{s}$.

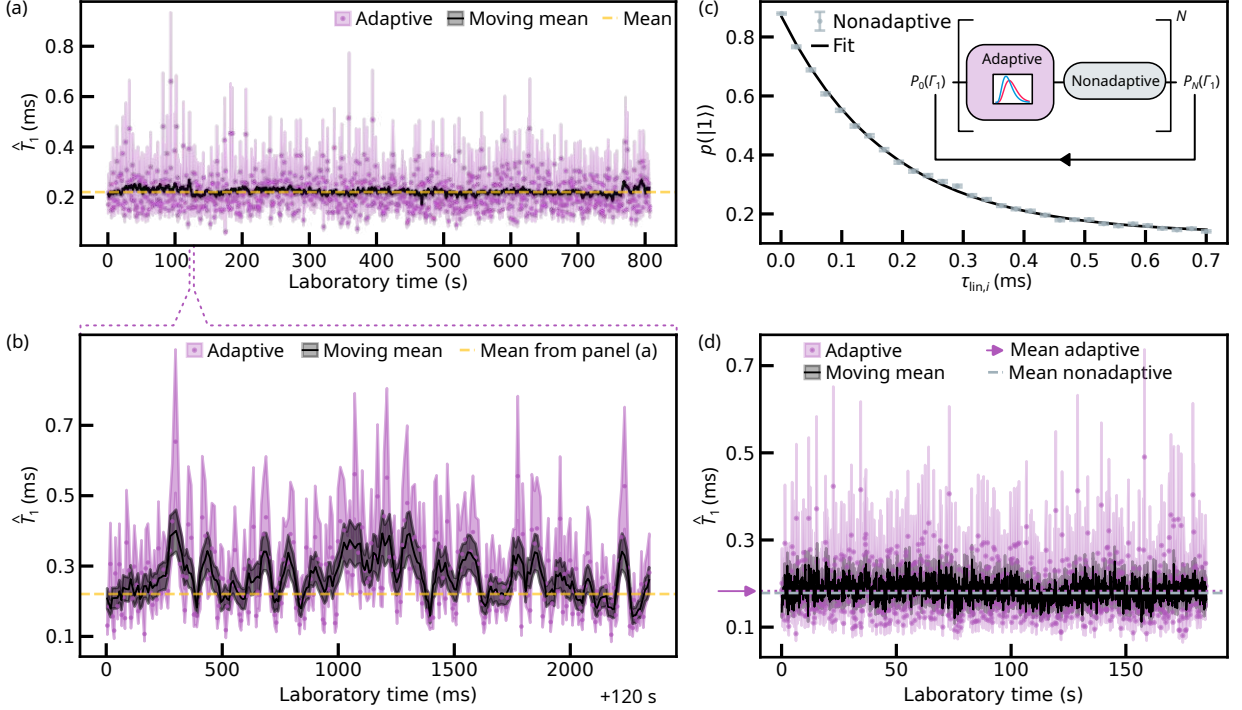


FIG. S3. **Tracking of the decay-rate fluctuations in Q₂ by adaptive estimation on the controller.** Reproducing Fig. 2 from the main text in Q₂. (a) Adaptive tracking with $N = 49$. Each purple point in this plot required an average measurement time of ≈ 8 ms. The moving average is over 300 samples. (b) Zoom-in at 120 s of panel (a) (purple dashed lines), where \hat{T}_1 shows fast switching with timescales on the order of tens of ms. (c) Inset: Interleaved adaptive and nonadaptive estimation sequence. Main panel: Experimental results for the nonadaptive protocol. (d) Experimental results for the adaptive tracking protocol, interleaved with nonadaptive estimates in the inset panel. Main panel: \hat{T}_1 (purple dots) of the final probability distribution $P_{29}(\Gamma_1)$ of the 10,000 estimates performed during the ≈ 164 s of the experiment. The black line is a moving average over 10 samples.

DECAY-RATE ESTIMATION IN Q₂

The aim of this section is to replicate the estimation protocols of Fig. 2 of the main text (Q₁) in another qubit (Q₂) in the same device for reproducibility. The qubit frequency of Q₂ is ≈ 3.8 GHz, the anharmonicity is ≈ -220 MHz and the associated readout frequency is 6.85 GHz. The drive line configuration in the cryostat is nominally identical to what shown in Fig. S1 for Q₁.

Adaptive estimation

Here we perform the adaptive estimation similarly to Fig. 2(a) of the main text. For plotting clarity in Fig. S3(a), we downsample by $D = 100$ the original trace of 100,000 estimates over 8.06×10^2 s of the experiment which used $N = 49$ single-shot measurements per estimation repetition. The black line represents a moving average of 300 samples. The dashed yellow line indicates the average $\bar{T}_1 \approx 220$ μ s over this dataset.

In Fig. S3(b), we replot the \hat{T}_1 timetrace of (a) around 120 s (purple dashed lines) where \hat{T}_1 switches between $\gtrsim 300$ μ s and ≈ 150 μ s on a timescale of tens of milliseconds. The moving average window consists of 5 samples. In Fig. S4 we plot different 10-second-long windows of the time trace shown in Fig. S3(a). The fluctuations show telegraphic switching between high values of $\hat{T}_1 > 400$ μ s and low values $\hat{T}_1 \approx 150$ μ s, with dwell times shorter than what measured in Q₁.

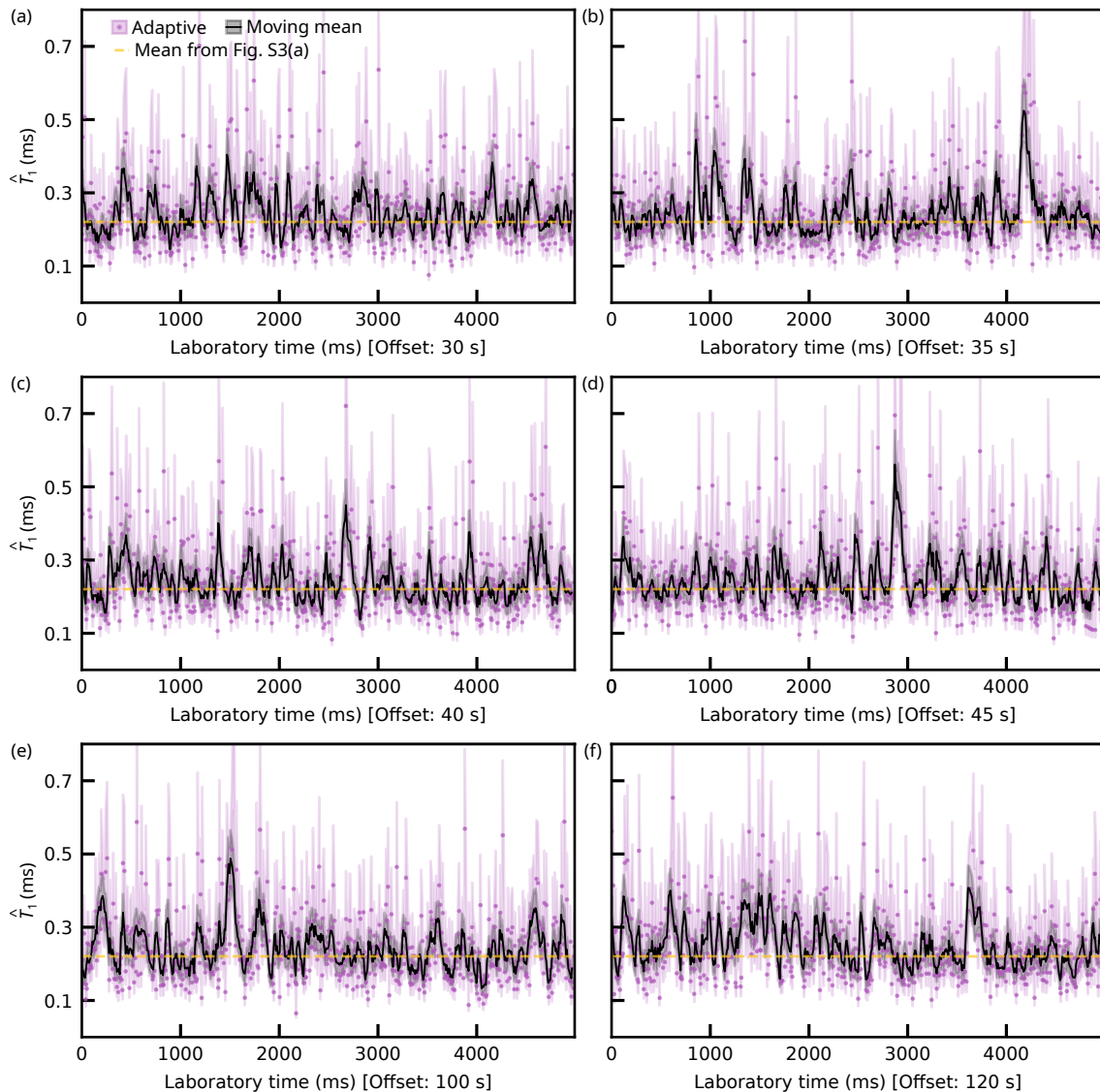


FIG. S4. **Adaptive estimation in Q_2 : additional examples of fast fluctuations** (a-f) Plotting not downsampled windows of Fig. S3(a), where \hat{T}_1 shows fast switching with timescales on the order of tens of milliseconds. Panel (f) includes Fig. S3(b).

Interleaved adaptive and nonadaptive estimations

The controller interleaves the adaptive probe cycles with nonadaptive ones [inset Fig. S3(c)], whose measurement outcomes $m_{\text{lin},i}$ are averaged and fitted as shown in the main panel of Fig. S3(c). The fit yields $T_1 = (178.3 \pm 1.7) \mu\text{s}$.

Regarding the duration of the probe cycle, the time used to read out the qubit is $\approx 3 \mu\text{s}$, and the time used to subsequently cool down the resonator again (to deplete it from any residual photons after the readout pulse) is $\approx 8 \mu\text{s}$. In this experiment $\alpha = 0.12$, $\beta = 0.13$ and the optimal waiting time in the i -th qubit cycles is given by $\tau_{i+1} \approx 1.0 \hat{T}_{1,i}$.

The controller is programmed to start with an initial gamma distribution prior with $(k_0, \theta_0) = (3, 550 \mu\text{s})$. In Fig. S3(d) we plot \hat{T}_1 and the black line is a moving average over 10 samples. The estimation cycle is repeated $N = 29$ times, while $\tau_{\text{lin},i}$ is increased linearly from $1 \mu\text{s}$ to $700 \mu\text{s}$. The adaptive estimation gives $\hat{T}_1 = (182.63 \pm 0.55) \mu\text{s}$ [purple arrow in Fig. S3(d)], computed from the mean and standard error of the adaptive time trace. The value is close to the one extracted from the fit $[(178.3 \pm 1.7) \mu\text{s}]$ [gray dashed line in Fig. S3(d)], with a slightly greater relative error compared to Fig. 2(d) of the main text. We attribute such small discrepancy to residual T_1 fluctuations between the interleaved probing cycles.

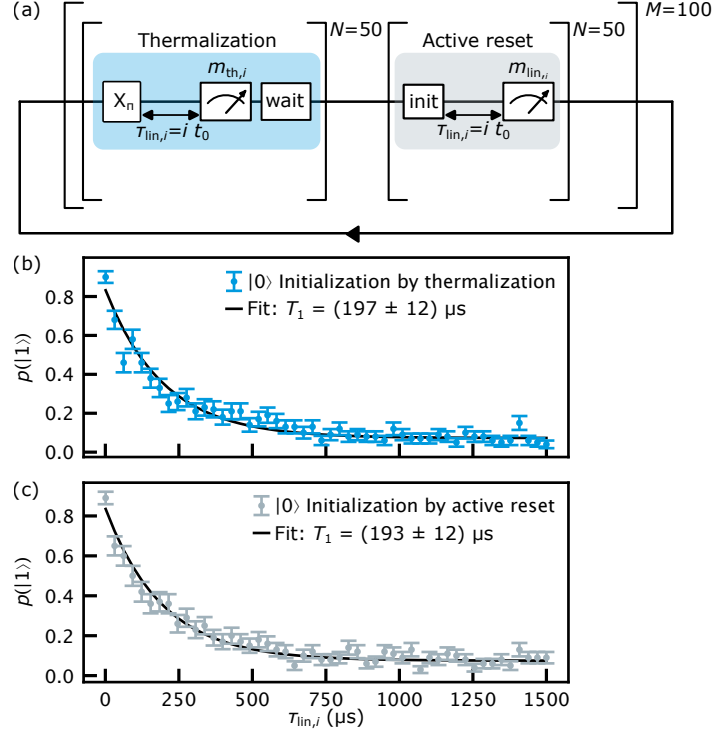


FIG. S5. **Interleaved T_1 measurement with and without active reset.** (a) One loop (solid arrow) represents a single repetition of the protocol. In this experiment, the controller performs $M = 100$ repetitions. At the beginning of each repetition, for each of the N probe cycles (Thermalization), labeled i , the controller initializes the qubit to the ground state by waiting 1.5 ms (wait), followed by an X_π pulse. It then waits for a linearly sampled time $\tau_{lin,i} = i\tau_0$ before measuring the qubit state ($m_{th,i}$). To test whether active reset affects the estimated T_1 value, the first $N = 50$ probing cycles are followed by another $N = 50$ cycles (active reset), where the qubit is initialized to the excited state via active reset, followed by an X_π pulse. The waiting times $\tau_{lin,i} = i\tau_0$ are used before measurement ($m_{lin,i}$). (b) Fraction of measured excited states $m_{th,i} = 1$ when the qubit is initialized to the ground state by thermalization. (c) Fraction of measured excited states $m_{lin,i} = 1$ when the qubit is initialized to the ground state by active reset and an X_π pulse. In panels (b) and (c) error bars represent the standard error from the experimental data.

INTERLEAVED ESTIMATIONS WITH AND WITHOUT ACTIVE RESET

Here we want to test whether active reset affects the T_1 estimation by, for instance, quasiparticle pumping [1]. As shown in Fig. S5(a), the experiment consists of $M = 100$ repetitions, where the controller performs $N = 50$ probe cycles with the qubit initialized to the ground state through thermalization by waiting 1.5 ms, followed by another $N = 50$ cycles where the qubit is actively reset to the excited state using a conditional X_π pulse. The measured fraction of excited states in each case is shown in panels Fig.S5(b) and (c), respectively. Panel (b) presents the results for thermalization-based initialization which yields $T_1 = (197 \pm 12) \mu\text{s}$, while panel (c) yields $T_1 = (193 \pm 12) \mu\text{s}$ when active reset is applied. As the two values agree within uncertainty, we conclude that active reset is unlikely to introduce systematic effects in the fluctuations of T_1 .

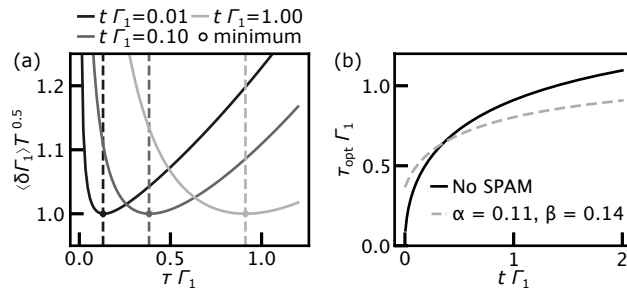


FIG. S6. **Optimal waiting time with binomial statistics** (a) Expected normalized standard deviation $\langle \delta \hat{\Gamma}_1 \rangle \sqrt{T}$ when $\hat{\Gamma}_1$ is estimated based on a series of probing cycles with fixed τ , the number of cycles being determined by a total time budget T . $\langle \delta \hat{\Gamma}_1 \rangle$ is plotted as a function of τ normalized by the relaxation rate Γ_1 . The curves differ by the idle time t that takes into account the finite reset and measurement time, normalized by Γ_1 . The global minimum of each curve (dot) provides the optimal τ that minimizes the uncertainty. (b) Optimal waiting time τ_{opt} as a function of the idle time t , both normalized by Γ_1 . The case without state and preparation measurement errors (SPAM) is the black curve where τ_{opt} approaches zero for sufficiently short idle times t . In the presence of SPAM (e.g. $\alpha = 0.11$ and $\beta = 0.14$, dashed-gray curve) τ_{opt} does not approach zero (see text).

OPTIMAL WAITING TIME WITH BINOMIAL STATISTICS

To estimate the relaxation rate as fast and precisely as possible, we first need to answer the following question: What is the locally optimal waiting time for estimating Γ_1 ? By “locally optimal” we mean within a greedy approach that minimizes both the experiment time and estimation uncertainty. To answer this question, we set aside the Bayesian framework and focus instead on the binomial statistics of the measurement outcomes for a fixed waiting time (i.e., the statistics of the number of successes for a number of independent trials), expanding on the main findings of Ref. [2].

In any estimation protocol, there are generally two regimes of interest. The first regime is where the waiting time is negligible compared to the “idle” time of each probing cycle (initialization, measurement, etc.). In this case, reducing the total measurement time involves optimizing the number of measurements. In the second regime, the waiting time is comparable to or exceeds the idle time. Here, one must determine whether it is more efficient to take a single measurement with an adaptively chosen long waiting time or to perform multiple shorter measurements within the same total measurement duration. In this section, we address this question, focusing on the latter regime where the waiting time is comparable to or much longer than the idle time, as in our experiment. The case of long idle times is discussed later.

Our goal is to determine the waiting time τ that reduces the variance of the estimate of Γ_1 most rapidly as a function of the total time T the estimation takes. For this purpose, we consider N consecutive single-shot measurements with waiting time τ , the outcomes of which are expected to follow a binomial distribution $B(N, p)$ with $p = \beta + (1 - \alpha - \beta)e^{-\Gamma_1 \tau}$ the probability to measure $|1\rangle$. Here Γ_1 is the parameter we want the controller to estimate, and α and β are misclassification probabilities for measuring $|0\rangle$ when at the beginning of the measurement the true state is $|1\rangle$ and measuring $|1\rangle$ when the true state is $|0\rangle$, respectively. When estimating p from a set of measurement outcomes, the expected standard deviation for the estimator \hat{p} due to the binomial measurement statistics is

$$\langle \delta \hat{p} \rangle = \sqrt{\frac{p - p^2}{N}}. \quad (\text{S.1})$$

It can be converted into a standard deviation for $\hat{\Gamma}_1$ based on these N measurement outcomes,

$$\langle \delta \hat{\Gamma}_1 \rangle = \frac{\sqrt{\tau + t}}{(1 - \alpha - \beta)\tau e^{-\Gamma_1 \tau} \sqrt{T}} \sqrt{\beta + (1 - \alpha - \beta)e^{-\Gamma_1 \tau} \sqrt{1 - \beta - (1 - \alpha - \beta)e^{-\Gamma_1 \tau}}}, \quad (\text{S.2})$$

where we used that $N = T/(\tau + t)$, with t the required idle time delay between one measurement and the next, and T the total time of the experiment. We see that $\langle \delta \hat{\Gamma}_1 \rangle$ decays $\propto 1/\sqrt{T}$, and by introducing the dimensionless variables $\tilde{\tau} = \Gamma_1 \tau$, $\tilde{t} = \Gamma_1 t$ and $\tilde{T} = \Gamma_1 T$ we derive an optimal measurement time $\tilde{\tau}^* = \tau_{\text{opt}} \Gamma_1$ by solving

$$\frac{\partial}{\partial \tilde{\tau}} \left(\frac{\sqrt{\tilde{\tau} + \tilde{t}}}{\tilde{\tau} e^{-\tilde{\tau}} \sqrt{\tilde{T}}} \sqrt{[\beta + (1 - \alpha - \beta)e^{-\tilde{\tau}}][1 - \beta - (1 - \alpha - \beta)e^{-\tilde{\tau}}]} \right) \equiv 0. \quad (\text{S.3})$$

Except for some limiting cases, the solution to this equation must be found numerically. This gives us the specific value of the prefactor c presented in the main text, which depends on SPAM coefficients (α, β) and qubit idle time \hat{t} normalized by Γ_1 . Note that the derived τ_{opt} is a function of the true Γ_1 , which is of course unknown.

In Fig. S6(a) we plot the uncertainty $\langle \delta \hat{\Gamma}_1 \rangle \sqrt{T}$, with minimum normalized to 1, for different values of idling time t with $\alpha = \beta = 0$. Each curve shows a different global minimum corresponding to the optimal waiting time τ_{opt} . In Fig. S6(b) we plot the numerically found τ_{opt} as a function of the idle time t , both normalized by the decay rate Γ_1 , in the absence and presence of state preparation and measurement (SPAM) errors. We see that in absence of SPAM (black curve) as $t \rightarrow 0$, the optimal waiting time $\tau_{\text{opt}} \rightarrow 0$. This reflects the fact that as the idle time is reduced, it is better to perform more measurements with very short waiting times. In the presence of SPAM (dashed-gray curve), as in the experiment of Fig. 2 of the main text with $\alpha = 0.11$ and $\beta = 0.14$, τ_{opt} does not approach zero. We notice this non-zero limit occurs only when $\alpha \neq 0$. On the other hand, by setting $\beta = 0$ and $t \rightarrow 0$, we find one of the few analytical solutions of (S.3), which is:

$$\tau_{\text{opt}} \Gamma_1 = 1 + \text{LambertW} \left(\frac{\alpha - 1}{e} \right), \quad (\text{S.4})$$

where the Lambert W function, also known as the product logarithm, is defined as the inverse relation of $f(w) = we^w$.

Adaptive waiting time implementation on the controller

Since solving Eq.(S.3) numerically on the controller is not feasible given the complexity of the calculation and the available numerical accuracy on the FPGA, we program as fixed prefactor c for the waiting time $\tau = c\hat{T}_1$ the one corresponding to $T_1 = 1/\Gamma_1 = 100 \mu\text{s}$, on the order of magnitude of the observed T_1 in our device. In the experiment in Fig. 2(a)[(d)] of the main text, the average idle time $t \approx 23.2 \mu\text{s}$ [345 μs]. This choice deviates by a factor of 4.3 [1.5] in Fig. 2(a)[(d)] of the main text from the optimal waiting time of Fig. S6 considering the average value of the estimated $\bar{T}_1 \approx 350 \mu\text{s}$ [135 μs]. For the prefactor c , the choice of $T_1 = 100 \mu\text{s}$ remains a conservative choice to better estimate shorter T_1 values, as, in a QPU, the primary concern is whether the fidelity exceeds a user-defined threshold required for quantum error correction. Even though we do not observe a difference in performance for different values of c , we choose to better estimate worst-case parameter fluctuations rather than best-case values. Due to the numerical precision of the controller, the actual ratio between τ_{i+1} and $\hat{T}_{1,i}$ varies slightly between probe cycles. A potential future improvement would be to precompute a lookup table of the numerically solved equation offline and upload it to the FPGA for real-time update of the prefactor c .

Optimal waiting time with the number of measurements

Here we show how the standard deviation of our decay rate measurements scales with the *number* of measurements performed during an experiment, neglecting that each measurement is time-dependent (in other words, we work in the limit $t \rightarrow +\infty$). The scheme is based on repeated measurements at the same sampling time t . These repeated measurements are averaged to produce a single data point, which is then used to estimate the parameter Γ_1 of the exponential distribution:

$$y(\tau) = \beta + (1 - \alpha - \beta) \exp(-\Gamma_1 \tau) \quad (\text{S.5})$$

To estimate Γ_1 , given an estimate of the excited state return probability y at some time τ , we determine which τ gives the smallest variance on our estimate of Γ_1 . Here, τ corresponds to the probing time at which the qubit is measured. Let the point be (y_0, τ_0) . The estimate of Γ_1 is found by inverting $y(\tau)$:

$$\Gamma_1 = -\frac{1}{\tau_0} \log \left(\frac{y_0 - \beta}{1 - \alpha - \beta} \right). \quad (\text{S.6})$$

The uncertainty in Γ_1 is determined by differentiating Eq. (S.6):

$$\delta \Gamma_1 = \left| \frac{d}{dy_0} \left(-\frac{1}{\tau_0} \log \left[\frac{y_0 - \beta}{1 - \alpha - \beta} \right] \right) \delta y_0 \right|. \quad (\text{S.7})$$

Calculating the derivative, we find:

$$\delta\Gamma_1 = \frac{1}{(y_0 - \beta)\tau_0} \delta y_0. \quad (\text{S.8})$$

Assuming we are measuring a qubit where N is the number of single-shot measurements, the uncertainty in y at (τ_0, y_0) due to binomial statistics is:

$$\langle \delta \hat{y}_0 \rangle = \sqrt{\frac{y_0 - y_0^2}{N}} \quad (\text{S.9})$$

We observe that the uncertainty of the sampled point decreases toward zero as y_0 approaches 0 and 1. This occurs when τ_0 approaches $+\infty$ and 0 if there are no SPAM errors (i.e. $\alpha = \beta = 0$), which are the limiting cases where we always measure the qubit in state $|0\rangle$ or $|1\rangle$. Inserting the relation between variation in y_0 and Γ_1 we find

$$\langle \delta \hat{\Gamma}_1 \rangle = \frac{1}{(y_0 - \beta)\tau_0\sqrt{N}} \sqrt{y_0 - y_0^2}, \quad (\text{S.10})$$

In the case of no SPAM errors, the uncertainty in $\hat{\Gamma}_1$ becomes:

$$\langle \delta \hat{\Gamma}_1 \rangle = \frac{1}{\tau_0\sqrt{N}} \sqrt{y_0^{-1} - 1}, \quad (\text{S.11})$$

and by substituting y_0 , we get:

$$\langle \delta \hat{\Gamma}_1 \rangle = \frac{1}{\tau_0\sqrt{N}} \sqrt{\exp(\Gamma_1\tau_0) - 1}. \quad (\text{S.12})$$

This expression describes the evolution of the uncertainty in the exponential parameter as a function of the number of samples N and the sampling time τ_0 . To minimize the uncertainty in Γ_1 , we solve:

$$\frac{d}{d\tau} \langle \delta \hat{\Gamma}_1 \rangle = 0. \quad (\text{S.13})$$

The optimal sampling point τ_0 is found to be:

$$\tau_{\text{opt}} = \frac{\text{LambertW}(-2e^{-2}) + 2}{\Gamma_1}, \quad (\text{S.14})$$

where the Lambert W function is the inverse relation of $f(w) = we^w$ as introduced in the previous section. Approximately, the optimal value is:

$$\tau_{\text{opt}} \approx 1.59\Gamma_1^{-1}. \quad (\text{S.15})$$

Using Eq. (S.12), the minimal uncertainty in Γ_1 is:

$$\langle \delta \hat{\Gamma}_1 \rangle_{\text{opt}} = \frac{\Gamma_1}{1.59\sqrt{N}} \sqrt{\exp(1.59) - 1} \approx \frac{1.24\Gamma_1}{\sqrt{N}} \quad (\text{S.16})$$

This result expresses the lowest achievable uncertainty as a function of the number of single-shot samples N . However, we recall that each measurement is inherently time-dependent, so it is more realistic to consider the time-dependent description of the previous subsection.

The analytical solution in (S.14) can be also be extended to the specific case of SPAM errors where $\beta = 0$, to get

$$\tau_{\text{opt}} = \frac{\text{LambertW}[2(\alpha - 1)e^{-2}] + 2}{\Gamma_1}. \quad (\text{S.17})$$

To our knowledge, there is no simple analytical solution for $\beta \neq 0$.

DECAY-RATE ESTIMATION WITH GAMMA DISTRIBUTIONS

In this section we derive the moment matching of the gamma distribution $\Gamma(k, \theta)$ presented in the main text. Let the qubit decay rate $\lambda \sim \Gamma(k, \theta)$. Its probability density function (pdf) reads

$$p(\lambda|k, \theta) = \frac{\theta^k}{\Gamma(k)} \lambda^{k-1} e^{-\theta\lambda} \quad (\text{S.18})$$

We make the prior assumption that $T_1 = 1/\lambda \sim \Gamma^{-1}(k, \theta)$, i.e., T_1 follows the inverse Gamma distribution. In the following, we will use $E[\cdot]$ to denote the expectation operator and refer to $X|Y$ as the random variable X conditioned on Y . Together, $E[X|Y]$ is the expectation of X after conditioning on Y .

Assuming the qubit is initialized to the (unobserved) excited state $s = 1$, the probability that a qubit is still in the excited state after waiting time τ is

$$P(s = 1|\tau, \lambda) = e^{-\lambda\tau} \quad (\text{S.19})$$

We can only observe the measured state m which can differ from s due to SPAM errors with error probabilities $\alpha = P(m = 0|s = 1)$ and $\beta = P(m = 1|s = 0)$. Here, we assumed that the SPAM error parameters are independent of T_1 and τ , as is commonly done in practice. Thus, we observe $m = 1$ with probability

$$P(m = 1|\tau, \lambda) = \beta P(s = 0|\tau, \lambda) + (1 - \alpha)P(s = 1|\tau, \lambda) = \beta + (1 - \beta - \alpha)e^{-\lambda\tau} \quad (\text{S.20})$$

$P(m|\tau, \lambda)$ can be written in the form $a_m - b_m e^{-\lambda\tau}$ with $a_m = (1 - m)(1 - \beta) + m\beta$ and $b_m = (1 - 2m)(1 - \alpha - \beta)$. After observing the value of the measurement m , the posterior distribution of λ can be written as (using Z as normalization constant of the posterior):

$$\begin{aligned} p(\lambda|k, \theta, m, \tau) &= \frac{1}{Z} p(\lambda|k, \theta) (a_m - b_m e^{-\lambda\tau}) \\ &= \frac{1}{Z} (a_m p(\lambda|k, \theta) - b_m p(\lambda|k, \theta) e^{-\lambda\tau}) \\ &= \frac{a_m p(\lambda|k, \theta) - b_m \left(\frac{\theta}{\theta + \tau}\right)^k p(\lambda|k, \theta + \tau)}{a_m - b_m \left(\frac{\theta}{\theta + \tau}\right)^k} \end{aligned} \quad (\text{S.21})$$

Note that if $a_m = 0$ (which is the case for $m = 1$ and $\beta = 0$), the posterior simplifies to the gamma distribution $p(\lambda|k, \theta + \tau)$. However, in general we have that after N measurements, the posterior is a linear combination of 2^N gamma distributions. In general, due to the law of large numbers, the posterior distribution will approach the normal distribution as $N \rightarrow +\infty$.

Since for $m = 1$ at low SPAM error rate, the posterior is still approximately gamma distributed and the gamma distribution also approaches the normal distribution as $k \rightarrow +\infty$, our approach is to approximate the posterior $p(\lambda|k, \theta, m, \tau)$ using a gamma distribution via moment matching. Moment matching makes sense in this case since it can be implemented on the FPGA-powered controller but also enables the right scaling behavior of mean and variance, and thus ensures that as $N \rightarrow +\infty$, $k \rightarrow +\infty$.

The first and second moments of the gamma distribution are given by

$$E[\lambda|k, \theta] = \frac{k}{\theta}, \quad E[\lambda^2|k, \theta] = \frac{k + k^2}{\theta^2} \quad (\text{S.22})$$

Moment matching computes the parameters k, θ based on the moments. For the gamma distribution, we obtain

$$\frac{1}{\theta} = \frac{E[\lambda^2|k, \theta]}{E[\lambda|k, \theta]} - E[\lambda|k, \theta], \quad k = \theta E[\lambda|k, \theta] \quad (\text{S.23})$$

Thus, by computing the moments of the posterior $p(\lambda|k, \theta, m, \tau)$ (using a_m, b_m as above), we can compute the param-

eters of the approximating gamma distribution. Direct computation of the moment gives:

$$\begin{aligned}
\mathbb{E}[\lambda|k, \theta, m, \tau] &= \frac{a_m \mathbb{E}[\lambda|k, \theta] - b_m \left(\frac{\theta}{\theta+\tau}\right)^k \mathbb{E}[\lambda|k, \theta + \tau]}{a_m - b_m \left(\frac{\theta}{\theta+\tau}\right)^k} \\
&= \frac{k a_m - b_m \left(\frac{\theta}{\theta+\tau}\right)^{k+1}}{\theta a_m - b_m \left(\frac{\theta}{\theta+\tau}\right)^k}, \\
\mathbb{E}[\lambda^2|k, \theta, m, \tau] &= \frac{a_m \mathbb{E}[\lambda^2|k, \theta] - b_m \left(\frac{\theta}{\theta+\tau}\right)^k \mathbb{E}[\lambda^2|k, \theta + \tau]}{a_m - b_m \left(\frac{\theta}{\theta+\tau}\right)^k} \\
&= \frac{a_m \frac{k+k^2}{\theta^2} - b_m \left(\frac{\theta}{\theta+\tau}\right)^k \frac{k+k^2}{(\theta+\tau)^2}}{a_m - b_m \left(\frac{\theta}{\theta+\tau}\right)^k} \\
&= \frac{k+k^2}{\theta^2} \frac{a_m - b_m \left(\frac{\theta}{\theta+\tau}\right)^{k+2}}{a_m - b_m \left(\frac{\theta}{\theta+\tau}\right)^k} \\
&= \mathbb{E}[\lambda|k, \theta, m, \tau] \frac{1+k}{\theta} \frac{a_m - b_m \left(\frac{\theta}{\theta+\tau}\right)^{k+2}}{a_m - b_m \left(\frac{\theta}{\theta+\tau}\right)^{k+1}}.
\end{aligned}$$

Both equations are programmed on the controller for the adaptive estimation.

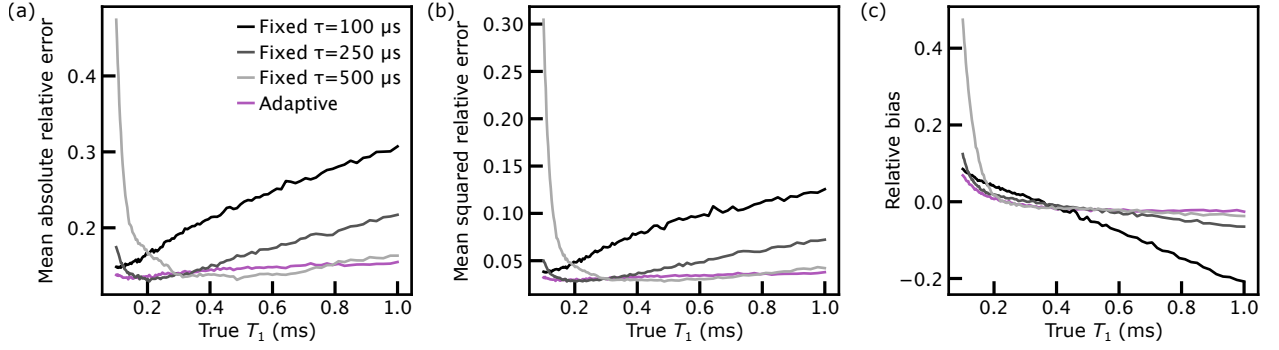


FIG. S7. **Comparison of nonadaptive and adaptive Bayesian methods** For each simulated true T_1 value we show the (a) mean absolute relative error $\langle |(T_1 - \hat{T}_1)/T_1| \rangle$, (b) mean squared relative error $\langle [(T_1 - \hat{T}_1)/T_1]^2 \rangle$, and (c) relative bias $\langle \hat{T}_1/T_1 \rangle - 1$, where the mean is computed over 20,000 trials (see text for parameters used in the simulation).

COMPARISON OF NONADAPTIVE AND ADAPTIVE BAYESIAN METHODS

In Fig. S7 we compare by simulation our adaptive method (purple lines) with a nonadaptive frequentist approach, where the waiting time τ is fixed (grayscale curves, with $\tau = 100 \mu\text{s}$, $250 \mu\text{s}$ and $500 \mu\text{s}$). We derive the frequentist approach as follows: We use the exact same probabilistic model with the same likelihood term (S.20) and prior (S.18). Using the sampled measurements $m_i \in \{0, 1\}$ obtained with waiting time τ , we then compute the maximum a-posteriori estimate

$$\hat{\lambda} = \arg \max_{\lambda} \left[\log P(\lambda | k_0, \theta_0) + \sum_{i=1}^N \log P(m = m_i | \tau, \lambda) \right],$$

and obtain the estimate $\hat{T}_1 = 1/\hat{\lambda}$. Note that the prior acts as a regularizer to the maximum log-likelihood estimate. This is necessary, since for low numbers of events $m_i = 1$ or $m_i = 0$ the maximum likelihood estimate of $\hat{\lambda}$ is either 0 or unbounded. Choosing the prior of our method as a regularizer allows for a fair comparison of the methods.

We plot the mean absolute relative error $\langle |(T_1 - \hat{T}_1)/T_1| \rangle$ (a), mean squared relative error $\langle [(T_1 - \hat{T}_1)/T_1]^2 \rangle$ (b) and the relative bias $\langle \hat{T}_1/T_1 \rangle - 1$ (c) as a function of the “true” T_1 over hundreds of microseconds spanned by our long-lived transmon qubits. For each true T_1 value, the mean is computed from 20,000 trials, where each trial consists of $N = 100$ single-shot measurements. Similarly to the experiments in the main text, in the simulation we set $\alpha = \beta = 0.12$, and for the adaptive estimation each trial always starts with the same gamma prior distribution with $(k_0, \theta_0) = (3, 450 \mu\text{s})$. The simulation does not take into account finite idle times t in the setup, thus we simply set $c = 1$ for the adaptive method.

The results show three points: (i) The adaptive choice of τ makes the algorithm robust with approximately constant low error rates (a,b), across the whole range of interest (hundreds of microseconds), while the frequentist method with fixed τ achieves similarly low errors only when $\tau \approx T_1$. (ii) Our method exhibits very low bias in the region $T_1 > 150 \mu\text{s}$ and the lowest absolute bias overall. For the region $T_1 < 150 \mu\text{s}$ bias is introduced via the choice of prior which only has little probability mass in this region. (iii) The approximated inference scheme using moment matching works very well and there is only little information lost.

HOW SPAM AFFECTS THE ESTIMATION PROTOCOL

To assess the influence of SPAM miscalibration on the adaptive Bayesian estimator, we fix the true SPAM parameters to $\alpha_{\text{sim}} = \beta_{\text{sim}} = 0.025$ and sweep the estimator values $\alpha = \beta$. The resulting bias and mean absolute relative error are shown in Fig. S8. Overestimating SPAM errors (larger α, β , lighter curves) consistently worsens performance across all T_1 . This is consistent with the estimator treating measurements as less informative, which slows the posterior update after each single-shot measurement and yields larger residual bias and variance after the fixed number of samples. Underestimating SPAM errors (smaller α, β , darker curves) leads to increased error primarily at small T_1 . In this regime the estimator overweights observed ground-state outcomes, effectively overestimating T_1 and producing

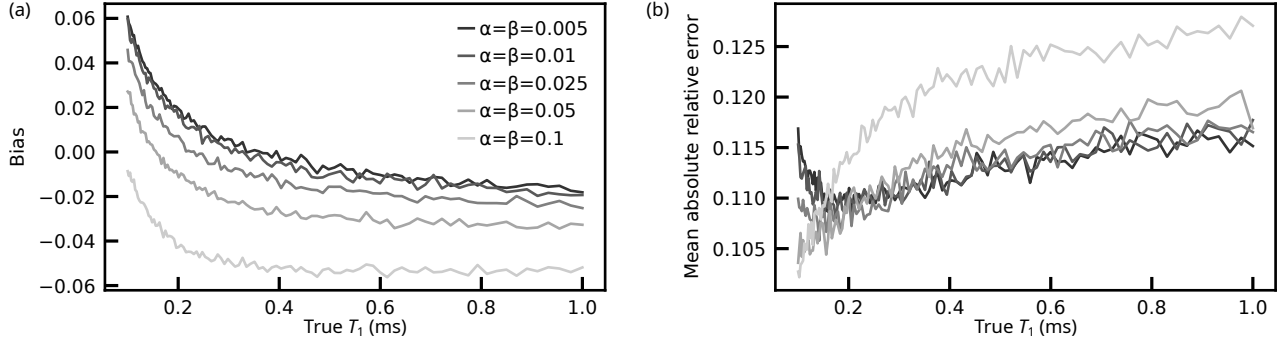


FIG. S8. **How SPAM affects the estimation protocol.** For each simulated true T_1 value we show (a) the relative bias $\langle \hat{T}_1/T_1 \rangle - 1$ and (b) the mean absolute relative error $\langle |(T_1 - \hat{T}_1)/T_1| \rangle$, computed over 10,000 trials and different values of $\alpha = \beta$. The true SPAM parameters are fixed to $\alpha_{\text{sim}} = \beta_{\text{sim}} = 0.025$, while the estimator uses mismatched values $\alpha_{\text{est}} = \beta_{\text{est}}$.

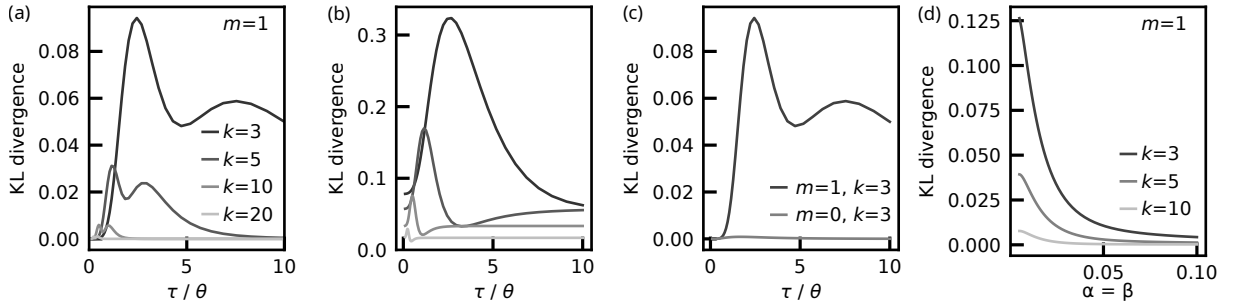


FIG. S9. **Comparison of exact posteriors with gamma and truncated-normal approximations.** For $\alpha = \beta = 0.01$, (a) KL divergence between the exact posterior and the gamma approximation as a function of τ/θ for several prior shape parameters k . The maximal deviation occurs for outcome $m = 1$ and decreases rapidly with increasing k . (b) Corresponding KL divergence for the truncated-normal approximation. (c) KL divergence for $k = 3$ comparing outcomes $m = 0$ and $m = 1$, showing that the gamma approximation is worse in the skewed $m = 1$ case, while updates with $m = 0$ remain very close to the gamma family. (d) Dependence of the KL divergence on the SPAM error probability, $\alpha = \beta$, evaluated at the worst-case τ for each k . Larger error rates reduce the measurement information and thus keep the posterior closer to the prior, improving the gamma approximation.

a positive bias visible in Fig. S8(a). Using the correct SPAM parameters ($\alpha_{\text{est}} = \beta_{\text{est}} = 0.025$) yields the smallest bias and lowest overall error [panel (b)].

VALIDITY OF THE GAMMA APPROXIMATION

KL divergence between exact and approximate posteriors The posterior after a single measurement depends only on the ratio τ/θ of the waiting time to the prior scale parameter. We therefore fix $\theta = 1$ without loss of generality [3] and compute the Kullback–Leibler (KL) divergence

$$D_{\text{KL}}(P_{\text{exact}} \parallel Q) = \int_0^\infty p_{\text{exact}}(\lambda) \log \left[\frac{p_{\text{exact}}(\lambda)}{q(\lambda)} \right] d\lambda, \quad (\text{S.24})$$

where P_{exact} is the exact posterior [Eq. (S.21)] Q is either the gamma approximation or the truncated normal approximation. The exact posterior can be evaluated in closed form as a linear combination of two gamma densities, whereas the approximations are obtained by matching the first two posterior moments.

Figure S9(a) shows the KL divergence between the exact posterior and the gamma approximation for the worst-case outcome $m = 1$, where deviations are largest, using $\alpha = \beta = 0.01$. We plot the divergence as a function of τ/θ for several prior shape parameters $k \in \{3, 5, 10, 20\}$. Two trends are apparent. First, the KL divergence is bounded and remains small ($\lesssim 0.1$) over the entire parameter range. Second, the approximation improves rapidly with increasing k , as expected because the posterior becomes sharply peaked and hence more Gaussian-like.

Comparison with a truncated normal approximation To verify whether the gamma choice is better with respect to a Gaussian distribution, we compare our moment-matched gamma approximation with a moment-matched truncated normal distribution. As shown in Fig. S9(b), the truncated normal typically exhibits a much larger KL divergence than the gamma function in (a), especially for small k where the posterior is skewed. This confirms that the gamma family captures the asymmetry of the posterior more faithfully than a normal distribution. Only for large k the two approximations become comparable, which is consistent with the central limit theorem.

Figure S9(c) compares the cases $m = 0$ and $m = 1$ for fixed $k = 3$. As expected, the approximation error is largest for $m = 1$, which shifts the posterior toward larger decay rates and produces a more asymmetric shape. In contrast, the $m = 0$ update preserves the overall shape of the prior and is therefore very well captured by a gamma distribution. We notice that for $\alpha = 0$, the gray line ($m = 0, k = 3$) is 0.

Dependence on SPAM Here we investigate how SPAM influences the quality of the approximation. To this end, we sweep $\alpha = \beta$ from 0.005 to 0.1, and evaluate the KL divergence at the value of τ that produces the worst-case approximation error for each k [identified from Fig. S9(a)]. As shown in Fig. S9(d), the KL divergence decreases monotonically with increasing error rates. This behavior is intuitively expected: for large α and β , the measurement contains little information and the posterior remains close to the prior, which is exactly gamma-distributed. Consequently, the gamma approximation is most challenged in the experimentally relevant regime of small but nonzero infidelity, yet even in this case the divergence remains below ≈ 0.1 .

In summary, the KL-divergence analysis supports three conclusions: (i) the gamma approximation provides an accurate representation of the exact posterior over a wide parameter range, with errors on the level of a few percent in KL divergence, (ii) it consistently outperforms a truncated normal approximation, particularly in the skewed, low- k regime, and (iii) the approximation improves both with increasing prior information (larger k) and with increasing measurement error rates, where the posterior approaches the gamma-distributed prior.

QUASISTATIC APPROXIMATION AND MARKOVIANITY

In this section we comment on the quasistatic approximation mentioned in the main text. We start by invoking standard derivation of Fermi Golden Rule, which amounts to a linear approximation of the exponential decay. Within this approximation the probability of occupying the ground state after the time t is given by:

$$P_0(t) \approx \frac{4|M_{01}|^2}{\hbar^2} \int_{-\infty}^{\infty} d\omega S_V(\omega) \frac{\sin^2((\omega - \omega_{01})t/2)}{(\omega - \omega_{01})^2} \quad (\text{S.25})$$

where $S_V(\omega)$ is the spectral density of the noise that couples to the qubit, and ω_{01} is the qubit frequency and $|M_{01}|^2$ is the matrix element for the transition. In this context, *Markovian* approximation is typically associated with the fact that the noise spectrum $S_V(\omega)$ is approximately constant over the bandwidth $\sim 1/t$ around ω_{01} . In this case the integral can be evaluated, yielding a constant rate $P_0(t) \approx \Gamma_1 t$, where $\Gamma_1 = 2\pi|M_{01}|^2 S_V(\omega_{01})/\hbar^2$.

This shows that a time-dependent rate, $\Gamma_1(t)$, can arise in three ways. First, the matrix element $|M_{01}(t)|^2$ is time-dependent, which does not affect the Markovian nature of the decay. Alternatively the power of the noise can be time-dependent due to either (i) change of the spectrum $S_V(\omega, t)$ or (ii) change of the qubit frequency $\omega_{01}(t)$. In both cases the decay remains Markovian as long as the noise is broadband on the scale $\sim 1/t$.

When $\Gamma_1(t)$ varies during the measurement, the master equation $\frac{d}{dt}P_0(t) = -\Gamma_1(t)P_0(t)$ has the solution:

$$P_0(t) = \exp\left(-\int_0^t \Gamma_1(t')dt'\right) = \exp(-\overline{\Gamma}_1 t) \quad (\text{S.26})$$

where $\overline{\Gamma}_1 = \frac{1}{t} \int_0^t \Gamma_1(t')dt'$ is the time-averaged decay rate over the measurement window t .

It shows that our Bayesian estimation, which fits an exponential decay to find a single rate, is measuring the time-averaged rate, $\overline{\Gamma}_1$, correctly capturing the mean decay effect even if the rate fluctuates rapidly during the measurement. Moreover, since $\Gamma_1(t)$ is a stochastic process, $\overline{\Gamma}_1(t)$ is a random variable. But this is also how Bayesian statistics treats an estimated variable, and so the method should be robust to whatever fast fluctuations are not resolved (which should just show up as some inherent uncertainty in the Γ_1 the controller is trying to estimate).

This allows us to clarify what our scheme estimates across different fluctuation timescales:

- **Slow Fluctuations** (slower than our total estimation time): Our scheme can successfully *track* these slow drifts in the average decay rate in real-time. This is the primary demonstration in our manuscript.
- **Fast Fluctuations** (much faster than the single measurement time t): Our scheme will yield a stable estimate of the mean decay rate $\langle \Gamma_1 \rangle$. The fast fluctuations are effectively averaged out during each measurement.
- **Intermediate Fluctuations** (timescale comparable to t): For fluctuations in this regime, each estimation shot witnesses a slightly different time-average. Presence of such fluctuations, might be responsible for generating uncorrelated outliers, if the prior distribution becomes too narrow. However, as shown empirically, such events are sufficiently rare.

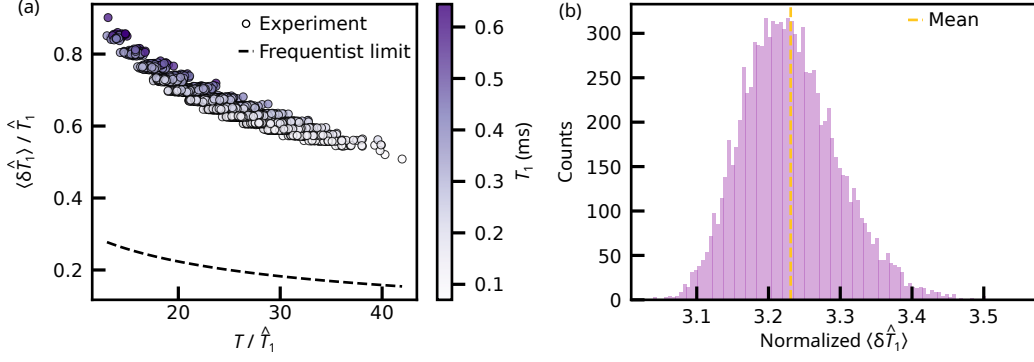


FIG. S10. **Theoretical estimation uncertainty limit.** (a) $N = 10,000$ experimental uncertainties $\langle \delta \hat{T}_1 \rangle$ (68% credible interval) as a function of total time budget T , both axes normalized by the corresponding \hat{T}_1 . The dashed line corresponds to the frequentist limit given by Eq. (S.29). (b) $N = 10,000$ experimental uncertainties normalized by the frequentistic limit, the average is represented by the dashed yellow line.

THEORETICAL ESTIMATION UNCERTAINTY LIMIT

In this section we test the performance of our Bayesian protocol compared to the ideal case in the absence of SPAM ($\alpha = \beta = 0$). Then the expected uncertainty from the estimation $\langle \Gamma_1 \rangle$ from Eq. (S.2) becomes:

$$\langle \delta \hat{\Gamma}_1 \rangle = \sqrt{\frac{1 - e^{-\Gamma_1 \tau}}{\tau T e^{-\Gamma_1 \tau}}} \quad (\text{S.27})$$

In the limit of negligible idle times in the setup, $t \rightarrow 0$ and thus $\tau_{\text{opt}} \rightarrow 0$ [cf. Fig. S6(b)]. Then one obtains what we refer to as the “frequentist limit”:

$$\langle \delta \hat{\Gamma}_1 \rangle \approx \sqrt{\frac{\Gamma_1}{T}}, \quad (\text{S.28})$$

which is equivalent to

$$\langle \delta \hat{T}_1 \rangle \approx T_1 \sqrt{\frac{T_1}{T}}. \quad (\text{S.29})$$

To compare the frequentist limit with the experimental Bayesian estimate, we perform 10,000 repetitions of adaptive Γ_1 estimations, using 30 single-shot measurements per repetition. The settings are the same as in Fig. 1(d) of the main text.

In Fig. S10(a), we plot the uncertainties $\langle \delta \hat{T}_1 \rangle$ obtained from 10,000 repetitions, each requiring an elapsed laboratory time of T of a few milliseconds. Both $\langle \delta \hat{T}_1 \rangle$ and T are normalized by their respective estimates \hat{T}_1 . The measured uncertainty scales as predicted by Eq. (S.29) (dashed line).

In Fig. S10(b), we present a histogram of the experimental uncertainties $\langle \delta \hat{T}_1 \rangle$ (68% credible interval), normalized by their corresponding frequentist limit $\langle \delta \hat{T}_1 \rangle$. On average, the Bayesian protocol yields an uncertainty approximately 3.23 times higher than the limit set by Eq. (S.29). We emphasize that the frequentist limit applies to an unbiased estimator, whereas in our case, the experimental uncertainty $\langle \delta \hat{T}_1 \rangle$ is strongly determined by the initial choice of the prior distribution.

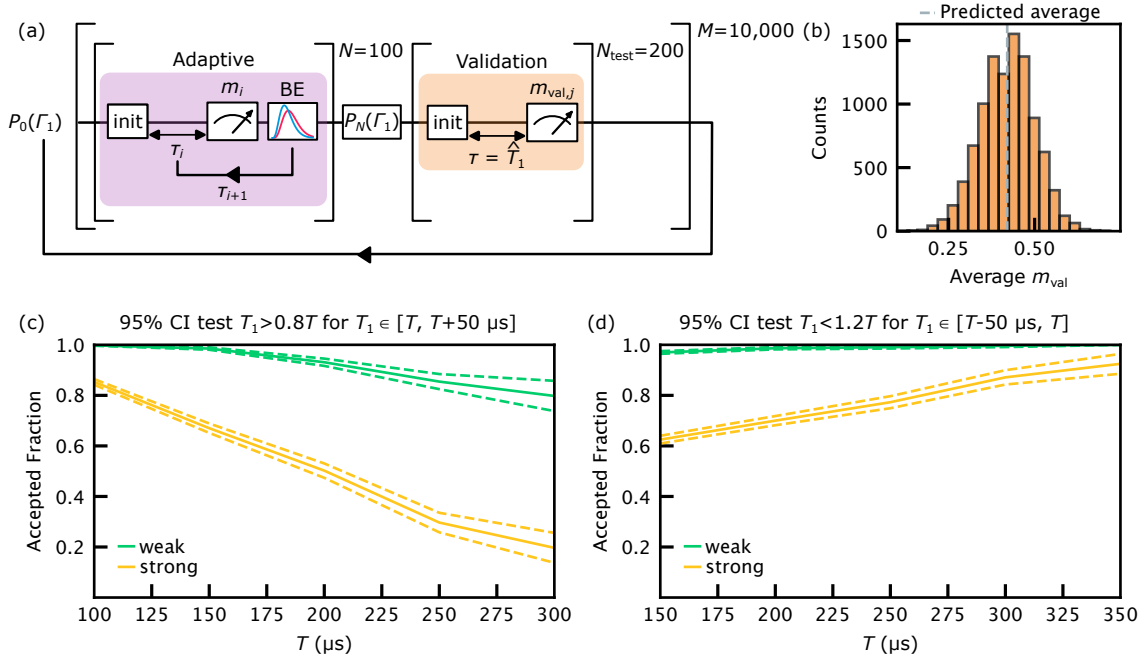


FIG. S11. **Validation of estimated values of T_1 .** (a) One loop (solid arrow) represents a single repetition of the validation protocol. In this experiment, the controller performs $M = 10,000$ repetitions. At the beginning of each repetition, the controller performs $N = 100$ adaptive probing cycles (Adaptive). To test whether the estimated T_1 is correct, the estimation sequence is followed by $N_{\text{test}} = 200$ cycles (Validation), where the qubit is initialized to the excited state and the same waiting time $\tau = \hat{T}_1$ is used before measurement ($m_{\text{lin},i}$). (b) Histogram of the number of counts of the average m_{val} extracted from each of the 10,000 validation sequences. The dashed line is the predicted average of the distribution based on the choice of $\tau = \hat{T}_1$. (c-d) Weak and strong tests (see text) to validate b: $T_1 > 0.8\hat{T}_1$, d: $T_1 < 1.2\hat{T}_1$.

VALIDATION OF ESTIMATED VALUES OF T_1

With a small number of measurements, we cannot obtain a sufficiently high precision estimate of T_1 . Thus, for practical applications, it is most important that if the algorithm returns a large value for the mean of the posterior \hat{T}_1 , the real value of T_1 is with high probability large enough to allow for higher-fidelity qubit operations. We therefore implemented statistical tests to validate that $T_1 > 0.8\hat{T}_1$ or, for the opposite direction, $T_1 < 1.2\hat{T}_1$, each indicating at most a 20% over- or underestimate.

We implement this as follows for the test of $T_1 > 0.8\hat{T}_1$, the other direction follows analogously. Let us assume the value of T_1 at the end of the runtime of the algorithm and during the test measurements is $T_1 = (1+q)\hat{T}_1$, for some $q \in (-1, 1)$. Then in our experiment with waiting time \hat{T}_1 and known SPAM error rates α and β the probability to observe state $m = 1$ is

$$P(m = 1|q) = \beta + (1 - \alpha - \beta) \exp\left(-\frac{1}{1+q}\right)$$

Under this assumption, the number of measurements with $m = 1$ among N_{test} measurements follows a binomial distribution, $S \sim \text{Binomial}(N_{\text{test}}, P(m = 1|q))$. If $T_1 > (1+q)\hat{T}_1$ we would expect to observe larger values of S on average (and smaller values for $T_1 < (1+q)\hat{T}_1$).

Based on this, we devised two statistical tests, which we call the “weak” and “strong” test. Assume we want to know whether $T_1 > (1+q)\hat{T}_1$ for some chosen value of q . For the weak test, we create 95% confidence interval $[S_{\text{weak}}, N_{\text{test}}]$ of the binomial distribution, i.e. $P(S \in [S_{\text{weak}}, N_{\text{test}}]) \geq 0.95$. If we observe $S < S_{\text{weak}}$, then the data provides evidence against the hypothesis that $T_1 > (1+q)\hat{T}_1$ and thus we conclude that the algorithm likely returned a false result. However, due to a limited number of validation measurements N_{test} we can take before device drift affects the results, and the presence of SPAM errors, we might not be able to reject many wrong results. For this reason, we then devised a second test, using the confidence interval $P(S \in [0, S_{\text{strong}}]) \geq 0.95$. With this, we accept the hypothesis only when $S > S_{\text{strong}}$. This test is equivalent to rejecting the counter hypothesis $T_1 < (1+q)\hat{T}_1$ and

thus the data provides evidence that T_1 is at least as large as tested. This test will tend to reject correct estimation results with small N_{test} .

To implement this framework, we perform the following experiment. For each repetition [see Fig. S11(a)], the controller executes $N = 100$ probing cycles to estimate T_1 , using a gamma prior distribution with parameters $(k, \theta) = (3, 450 \mu\text{s})$. After the estimation sequence, a validation sequence follows. During the validation, the controller performs $N_{\text{test}} = 200$ qubit cycles, initializing the qubit in the excited state and setting the waiting time to the estimated \hat{T}_1 from the previous adaptive probing sequence. After waiting for $\tau \approx \hat{T}_1$, the qubit state is measured and classified as $m_{\text{val},j}$.

The interleaved adaptive and validation sequences are repeated $M = 10,000$ times. In this experiment, we set $\alpha = 0.105$ and $\beta = 0.14$. Figure S11(b) shows a histogram obtained by binning the average $\langle m_{\text{val}} \rangle$ over $j = 1, 2, \dots, 200$ for each of the 10,000 validation sequences. The distribution is approximately centered around the expected probability $p = \beta + (1 - \alpha - \beta)e^{-1} \approx 0.418$ of measuring the excited state after setting $\tau \approx 1/T_1$ [dashed line in Fig. S11(b)].

For the test, we then partition the data and select the experiments for which \hat{T}_1 falls in an interval $[T, T + 50 \mu\text{s}]$ for $T \in \{100, 150, 200, 250, 300\} \mu\text{s}$ (the proportion of estimation results outside this interval is too small to evaluate). For all instances of the experiment in such interval, we compute the weak and strong tests validating the hypotheses $T_1 > 0.8T$ and $T_1 < 1.2T$ and record the fraction of passed tests as well as their 95% confidence interval based on the normal distribution.

The results [see Fig. S11(c-d)] show that for both experiments the weak test succeeded in between 80% to 100% of the estimation results in each interval. Thus, for the vast majority of the results the estimation errors are not so large that $N_{\text{test}} = 200$ samples can reject the hypothesis that the estimation error is below 20%. However, for the strong test, we see a much lower acceptance rate, i.e., the estimation errors are also not small enough to reject the opposite hypothesis that the error is larger than 20%. We can see in both cases that the fraction of accepted results increases towards more extreme results of \hat{T}_1 . Thus, Fig. S11(c) indicates that with increasing value of estimated \hat{T}_1 , the estimation error increases, as expected from Eq. (S.29). For those intervals with large T , the fraction of successful tests Fig. S11(d) is also increasing. Both tests indicate that large values of \hat{T}_1 might be overestimates of T_1 . The opposite holds for the other extreme for $T \leq 200 \mu\text{s}$, thus small values of \hat{T}_1 might be underestimates.

However, these results do not take into account the possible drift of T_1 during the validation measurements. Especially for large \hat{T}_1 , taking $N_{\text{test}} = 200$ validation samples can take a long time. For example for $\hat{T}_1 = 250 \mu\text{s}$, the time taken to estimate a validation sample is 55 ms in addition to the algorithm runtime. Thus, device drift may have already changed the results. This might be consistent with the smaller number of rejected samples with small T_1 which can take the samples in approximately half the time.

FREQUENCY OF EVENTS OF LARGE SWITCHES IN T_1

In this section we describe the analysis mentioned in the Section IV.C (Power spectral density and Allan deviation) of the main text where we conclude that switches in T_1 greater than $100\ \mu\text{s}$ on average occur once every 7.7 s.

To better understand the estimation errors of our algorithm and the fine-grained structure of the noise on T_1 , we partition all the single-shot outcomes of the 3-day-long time trace of Fig.3(a) of the main text into intervals of maximum length 200 ms. We ensure that partitioning only occurs after the controller completes an estimation repetition, as the single-shot outcomes within a repetition are not statistically independent due to their waiting times depending on previous outcomes. Since each estimation repetition is initialized with a prior independent of previous results, the repetition estimates are statistically independent. Within each interval, we split the estimates into a training and test set by assigning every second repetition run to the training set (e.g., runs 1, 3, 5, ...) and the remainder to the test set (e.g., 2, 4, 6, ...). We average the T_1 estimates from the training set to obtain an interval-wise estimate of the mean \bar{T}_1 .

Next, we identify pairs of consecutive intervals that satisfy the following criteria: (a) the average \bar{T}_1 in both intervals lies within the range $100\ \mu\text{s} < \bar{T}_1 < 400\ \mu\text{s}$, and (b) the difference between the average \bar{T}_1 values of the two intervals exceeds $100\ \mu\text{s}$. These thresholds are based on an independent validation, showing that individual estimates in this range have an error below 20% with high probability. This filtering step retains 3.8% of all 200 ms intervals.

We then use the corresponding test sets to evaluate whether the difference in \hat{T}_1 is statistically significant. Let \hat{T}_1^L and \hat{T}_1^R denote the \hat{T}_1 estimates of the left and right intervals, respectively, and T_1^L , T_1^R their unknown true values. Assuming without loss of generality that $\hat{T}_1^L < \hat{T}_1^R$, we perform two one-sided hypothesis tests: one to reject $H_0 : T_1^L > \hat{T}_1^R$ using the left interval's test data, and one to reject $H_0 : T_1^R < \hat{T}_1^L$ using the right interval's test data. Each test is performed at a 97.5% confidence level, and a switch is considered verified when both tests succeed.

Out of the 3.8% of intervals that pass the initial filter, 69% yield a verified switch, corresponding to approximately 2.6% of all intervals. This translates to one T_1 switch (exceeding $100\ \mu\text{s}$) every 7.7 s on average. Note that the analysis is constrained by the limited sampling rate, especially for large \hat{T}_1 values, as the algorithm's runtime scales approximately linearly with \hat{T}_1 due to longer waiting times.

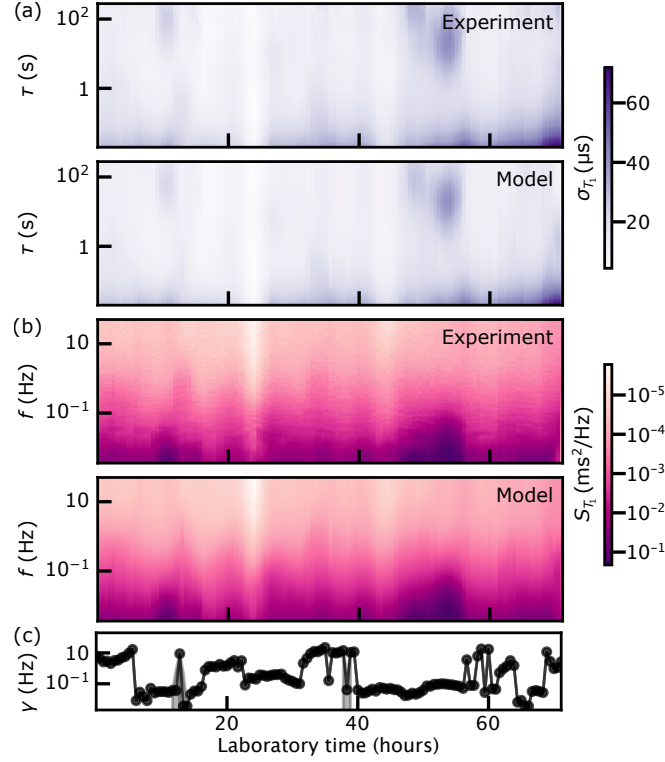


FIG. S12. **Comparing Allan deviation and PSD of T_1 time series with fit.** (a) Extracted and fitted Allan deviation for the 72-hour-long estimates using 2.7-hour-long time intervals. (b) Extracted and fitted PSD for the 72-hour-long estimates using 2.7-hour-long windows with 80% overlap. (c) Switching rates γ of the Lorentzian model used to fit the experimental data in panels (a, b).

FIT TO ALLAN DEVIATION AND POWER SPECTRAL DENSITY

In this section we provide more details on the fit used for Fig. 3 and 4 of the main text. We treat the estimated values of \hat{T}_1 as a stationary time series data and analyze the noise correlation using the power spectral density (PSD), defined as:

$$S_{\hat{T}_1}(f) = \int_{-\infty}^{+\infty} R_{\hat{T}_1}(\tau) e^{-2\pi i f \tau} d\tau, \quad (\text{S.30})$$

where $R_{\hat{T}_1}(\tau) = \langle \hat{T}_1(\tau) \hat{T}_1(0) \rangle$ is the autocorrelation function of the estimated \hat{T}_1 values, and $\langle \dots \rangle$ denotes the average over the sequence of estimated \hat{T}_1 values. To estimate the PSD, we use the Welch method, which divides the time series data into overlapping segments and computes the PSD for each segment. The PSD is then averaged over all segments to obtain the final estimate. The spectral density obtained for the 72-hour dataset is shown in Fig. 3(b) of the main text.

As discussed in the main text, the obtained PSD is dominated by $1/f$ noise, with a spectrum $S_{T_1}(f) = A_1/f$, suggesting the presence of low-frequency drift in the relaxation time. However, such a $1/f$ -dominated PSD does not provide meaningful insight into other noise sources. For this reason, we also compute the Allan deviation, a method for measuring frequency stability, defined as:

$$\sigma_{\hat{T}_1}(\tau) = \sqrt{\frac{1}{2\tau^2} \left\langle \left(\hat{T}_1[(n+2)\tau] - 2\hat{T}_1[(n+1)\tau] + \hat{T}_1[n\tau] \right)^2 \right\rangle}, \quad (\text{S.31})$$

where $\hat{T}_1[n\tau]$ is the estimated \hat{T}_1 at the n -th time point. The Allan deviation is shown in Fig. 3(c) of the main text. In Fig. S12, we plot the comparison between the measured and fitted Allan deviation [panel (a)] and PSD [panel (b)], as well as the fitted switching rate γ [panel (c)] for the Lorentzian process. The visual comparison of the experiment

and model, along with the small uncertainty in γ , show that the fit captures the main features of the fluctuations in the estimated \hat{T}_1 values.

* Current address: Research Laboratory of Electronics, Massachusetts Institute of Technology, Cambridge, MA 02139, USA; fabrizio.berritta@mit.edu

† mkjaergaard@nbi.ku.dk

- [1] S. Gustavsson, F. Yan, G. Catelani, J. Bylander, A. Kamal, J. Birenbaum, D. Hover, D. Rosenberg, G. Samach, A. P. Sears, *et al.*, Suppressing relaxation in superconducting qubits by quasiparticle pumping, *Science* **354**, 1573 (2016).
- [2] F. Leveraro, *Novel techniques for fast and precise estimation of qubit decay rates*, Master's thesis, University of Copenhagen (2024).
- [3] This will not influence the quantitative outcome of the integral, since it merely rescales the integration axis. The key point is that a change of θ only leads to a scaling of λ , i.e., it is a linear transformation of the $\theta = 1$ case. This holds for both the exact distribution and our moment matching. It then follows that the KL divergence is invariant under affine transformations of the compared random variable.